Suspended sediment fluxes in a shallow macrotidal estuary

Susanne Moskalski, France Floc'H, Romaric Verney

To cite this version:

Susanne Moskalski, France Floc'H, Romaric Verney. Suspended sediment fluxes in a shallow macrotidal estuary. Marine Geology, 2020, 419, pp.106050. ⟨10.1016/j.margeo.2019.106050⟩. ⟨hal-02353241⟩

HAL Id: hal-02353241
https://hal.science/hal-02353241v1

Submitted on 13 Apr 2021

Marine Geology
January 2020, Volume 419, Pages 106050 (20p.)
https://doi.org/10.1016/j.margeo.2019.106050
https://archimer.ifremer.fr/doc/00588/70046/

Suspended sediment fluxes in a shallow macrotidal estuary

Moskalski Susanne [1, *], Floc'h France [1], Verney Romaric [2]

[1] Université de Bretagne Occidentale, Institut Universitaire Européen de la Mer, LabexMER, Rue Dumont d'Urville, 29280 Plouzané, France
[2] Ifremer Centre Bretagne, ZI de la Pointe Diable, CS 10070, 29280 Plouzané, France

* Corresponding author : Susanne Moskalski, email address : Susanne.moskalski@stockton.edu

Abstract :

Residual suspended sediment flux in estuaries is dependent on water level, velocity, and suspended sediment concentration (SSC), but complex interactions between these variables and other forcing mechanisms can lead to drastic differences in the magnitude and direction of sediment flux. The goal of this study was to quantify residual suspended sediment flux in a shallow, macrotidal estuary, and to determine its most important forcing mechanisms, using the Dyer flux decomposition equation and a simplified analytical model. Water level, velocity, and acoustic backscatter were measured in the Aulne River estuary in Brittany, France, and acoustic backscatter converted to SSC. The vertical tide was slightly flood dominant near the mouth, but strongly flood dominant upstream. Velocity was ebb dominant throughout the estuary. The magnitude and direction of total residual suspended sediment flux changed with position in the estuary and seasonally. The Eulerian flux was dominant at the mouth, but the tidal pumping and Stokes drift components increased in importance landward. Residual suspended sediment flux in the Aulne is dependent on several processes in addition to those included in the simplified model. The strong spring-neap control and tidal resuspension of sediments in the Aulne and the presence of higher-order tidal velocity terms contribute in a non-negligible way to residual suspended sediment flux. Finally, all of the first five components of the Dyer flux decomposition equation are needed to accurately represent residual suspended sediment flux in the Aulne.

Highlights

► Magnitude and direction of total residual flux change with position and discharge. ► Eulerian flux is the main component of total flux near the mouth. ► Tidal pumping and Stokes drift flux components gain importance landward. ► The 6 processes in the model are insufficient to replicate residual flux in Aulne. ► First 5 Dyer flux components were all needed to estimate total residual flux.

Keywords : estuaries, estuarine processes, sediment flux decomposition, Brittany, Europe

1. Introduction

Suspended sediment flux quantifies the import, export, or transfer of suspended sediment in an estuary. It is calculated in an estuary from timeseries of current velocity and suspended sediment concentration (SSC). Sediment flux can be landward or seaward, and can change magnitude and direction with time, with position in an estuary, or due to changes in tidal forcing, freshwater discharge and meteorological phenomena (Friedrichs and Perry, 2001; French et al., 2008).

Directionality of suspended sediment flux in an estuary develops due to asymmetries in the tidal velocity or other distortions of the tidal wave. In shallow estuaries, where the tidal amplitude is more than one tenth of the mean water depth, flood or ebb dominance in water velocity can develop due to friction with the bottom or large changes in intertidal storage area with the tides (Friedrichs and Aubrey, 1988). Friction-induced distortion can also cause an asymmetry in the duration of the slack water periods after flooding and ebbing (Dronkers, 1986). Given the settling velocity of suspended sediment particles, velocity dominance or slack period asymmetry can produce a landward or seaward residual transport of sediment in an estuary.

Macrotidal estuaries share these characteristics of suspended sediment flux with microtidal and mesotidal estuaries, but tidal processes gain in importance. The large tide range in macrotidal estuaries brings with it strong tidal velocities that are capable of resuspending bottom sediment, and generating stronger mixing on flood (Allen et al., 1980). The tide tends to become increasingly distorted with distance landward in favor of flood dominance and a slack period asymmetry, where the slack after flood is longer (Allen et al., 1980). The final result is landward sediment transport and trapping. Macrotidal estuaries can, however, be ebb-dominant when wide intertidal zones are flooded regularly at high tide (Lessa, 1996). The spring-neap variability in tide range produces large changes in tidal prism volume, and hence also large changes in the degree of mixing and stratification (Allen et al., 1980). The spring-neap cycle also enhances the tide range and tidal velocities, leading to increased sediment resuspension during spring tides and deposition during neaps (Allen et al., 1980).

Suspended sediment flux can be calculated from velocity and suspended sediment concentration:

$$F(z) = U(z)C(z), \quad (1)$$

where *C* is SSC, *U* is the velocity, and *z* indicates the vertical coordinate. Flux calculated from the measured timeseries is called Instantaneous Flux, which can be lowpass filtered to eliminate tides (and then called Residual Flux). Flux calculated according to Equation 1 will hereafter be referred to as "Simple Flux" to differentiate it from the decomposition and modeling methods also used in this paper. Residual Simple Flux can be decomposed as follows (Dyer, 1997):

$$F = C_0U_0H_0 + C_0\overline{U_tH_t} + U_0\overline{H_tC_t} + H_0\overline{U_tC_t} + \overline{C_tU_tH_t} + H_0\langle\overline{U_dC_d}\rangle + H_o\langle\overline{U_{dt}C_{dt}}\rangle \quad (2)$$

F1 F2 F3 F4 F5 F6 F7

where *H* is the water level, subscript *0* indicates the tidal cycle mean value, subscript *t* indicates deviations from the tidal cycle mean, subscript *d* indicates deviations from the vertically averaged value, and subscript *dt* indicates deviations from the tidally averaged vertical mean. Angled brackets denote depth averages and overbars denote tidal cycle averages.

Term F1 is the Eulerian flux, and is the flux due to processes such as river discharge that occur on longer-than-tidal timescales. F1 is controlled by tidally averaged velocity, SSC, and water level. F2 is the flux due to Stokes drift on the tide, and is controlled by the phase difference between the M2 stage and velocity. These two comprise the advective terms. F3, F4, and F5 are the tidal pumping terms. F3 flux is induced by interactions between water level and SSC. F4 is sometimes called the dispersive flux, and is caused by complex interactions between SSC and velocity. F5 is controlled by the amplitude of the M2 water level, phase differences between velocity and water level, and the phase lag of SSC. F6 and F7 are vertical flux terms. F6 is the flux induced by tidally averaged vertical circulation, and F7 is related to vertical differences in SSC and velocity. Flux components calculated from Equation 2 will hereafter be called "Dyer Fluxes."

Due to the complexity of suspended sediment flux and the large number of forcing mechanisms with the potential to affect it, several researchers have attempted to simplify the analysis of sediment flux with models. The analytical model developed by Yu et al. (2012) calculates the residual suspended sediment flux (*F* on the left side of Equation 2) that is due to six particular forcing mechanisms only: the mean water depth; the M2 horizontal tidal amplitude; the residual, M2, and M4 tidal velocities; and the depth-averaged SSC gradient. The Yu model calculates the first five flux terms from the Dyer equation (F1 through F5), giving one depth-average value per tidal cycle for each term. The flux components F1 through F5 generated by the Yu et al. (2012) model are the same components as in the Dyer equation (Equation 2), but simplified to include only the five particular forcing mechanisms mentioned above. Flux components generated by the Yu model will hereafter be called “Yu Fluxes.”

The Yu et al (2012) model incorporates six specific forcing mechanisms that are often found to be the most important in estuaries, but additional possible forcing mechanisms can affect sediment flux, such as higher-order tidal frequencies and weather effects (Grasso et al., 2018). These are not accounted for by the Yu model, but if present they will affect the residual flux through their effects on the timeseries of velocity or suspended sediment concentration. Comparing the flux components calculated by the Yu model to the flux components calculated by the Dyer equation therefore provides an opportunity to discover the importance of the forcing mechanisms not included in the Yu model to the suspended sediment transport processes in a macrotidal estuary. It was for this reason that the Yu model was chosen to use in the study.

In this study we analyzed residual suspended sediment fluxes (following Dyer, 1997) and related variables in the shallow, macrotidal Aulne River estuary in northwestern France, and compared them to a simplified analytical model of residual suspended sediment flux (Yu et al., 2012). The goal was to quantify the magnitude and direction of the residual suspended sediment flux and to answer these questions:

1. What forcing mechanisms are dominant in the Aulne River estuary?
2. How much, if any, of the flux components and the total residual Simple Flux are not explained by the Yu et al. (2012) model?
3. Which Dyer flux components are needed to most closely estimate total residual Simple Flux?

The results demonstrate temporal and spatial variability of residual suspended sediment flux, and warn of the dangers of ignoring “minor” Dyer Flux components.

2. Materials and methods

2.1 Study Area

The Aulne River estuary is a shallow, macrotidal tributary of the Bay of Brest in western Brittany (Figure 1). The average freshwater discharge is 24 $m^3 s^{-1}$, with a maximum in February and minimum in August (Allen et al., 1980). The estuary occupies the lowermost 30 km of the river, and it is forced to end by a dam at Guily-Glaz. The maximum channel depth decreases from 18 m at the mouth to 2.5 m near the dam, and the bankfull width decreases from 265 m to 70 m. The tide range in the Bay of Brest is a minimum of 1.3 at neap tide and a maximum of 7.3 m during spring tide, and the spring tide range decreases to 4.5 m at Guily-Glaz. The watershed is dominated by agriculture, and the Aulne is the dominant contributor of suspended sediment to the Bay of Brest (Allen et al., 1980; Acolas et al., 2006). The area around Brest has a temperate climate with a strong oceanic influence. For the period 1981-2010, monthly average temperature ranged between 11° and 19° C, and the average precipitation was 1126 mm per year, with slightly more precipitation in winter than in summer (source MeteoFrance). Mean monthly wind speed varied 3.6 and 5 m s^{-1}, and direction varied seasonally but was predominantly from the west and southwest (source MeteoFrance).

The estuary is partially mixed/periodically stratified with a turbidity maximum zone controlled and maintained by tidal resuspension of bottom sediments and present only during spring tides (Bassoullet, 1979; Allen et al, 1980). The Aulne is well- or partially-mixed during spring tides and stratified during neaps. The river discharge also affects stratification, with well-mixed conditions more likely during low discharges, and full or partial stratification during higher river discharges due to the greater fresh water input (Pritchard, 1955; Hansen and Rattray, 1965). Tidal currents are roughly symmetrical near the mouth of the estuary, and become progressively distorted and flood dominant with distance landward. A slack period asymmetry also becomes increasingly prominent with distance landward, with the slack after flooding being much longer than the slack after ebbing. Residual circulation in the estuary is enhanced by greater density stratification during neap tides (Bassoullet, 1979; Allen et al, 1980).

2.2 Field and lab methods

Moored instruments were deployed for 3 weeks at two locations in the Aulne estuary in February and September 2013. The moorings were complemented by shipboard surveys at 4 locations (Figure 1, Table 1). February deployments began on 8 February 2013 at Site 3 and 11 February 2013 at Site 1, and ended on 4 March 2013 at both sites. In September the deployments lasted from 3 to 21 September 2013 at both sites. Moored instruments included acoustic Doppler current profilers and YSI pressure, turbidity, and salinity sensors. Anchor station profiling was conducted on three days in February and 7 days in September with a YSI.

A Nortek AWAC current profiler (frequency 1 MHz) was deployed along with a YSI 6290 V2 at Station 1, near the mouth of the Aulne. The AWAC was programmed to measure a 2-minute burst average at 1Hz every 5 minutes for profiles of currents and backscatter. The instrument was deployed in a Nortek mooring frame, which placed the top of the instrument head 0.62 m above bottom. The instrument was moored along the south side of the channel due to local government permit requirements, and the channel depth at the mooring site was 12 m in February and 10 m in September. The YSI was fitted with depth, conductivity, temperature, and turbidity sensors. The turbidity sensor of the YSI was calibrated before deployment to Hach Formazin Turbidity Standard at 4000 NTU, diluted to 400 and 1000 NTU. The YSI was programmed to take 1 measurement every 5 minutes, and was moored approximately 10 m away from the AWAC at a height of 1.4 m above bottom.

An RD Instruments Workhorse Acoustic Doppler Current Profiler (ADCP, 1.2 MHz) was deployed along with a YSI 6290 at Station 3. The ADCP was programmed to measure a 2-minute burst average at 1 Hz every 5 minutes for profiles of currents and backscatter. The instrument was deployed in a Barnacle mooring frame, which placed the instrument head 0.45 m above bottom. The channel depth at the mooring site was 4 m, and in the deepest part of the channel just off the center. The YSI was calibrated and programmed as described above for the YSI accompanying the AWAC.

Water samples and YSI profiles of turbidity and salinity were collected while anchored in a small vessel on a separate day at each site during spring tide in February; in September neap tide profiling was added for two sites. Profiling could only take place during daylight hours, resulting in approximately 6 hours of profiling and 8 profiles in February, and 9 hours and 29-36 profiles in September. Turbidity and salinity profiles were collected every 30 minutes in February and every 15 minutes in September with a YSI 6290 V2, calibrated as above. The YSI was programmed to sample continuously at 1 measurement per second. Water samples were collected from 20 cm below the surface by hand and from 50 cm above bottom via weighted Niskin bottle. Near-surface and near-bottom samples were collected every 30 minutes in February and every 60 minutes in September, except when the water depth was less than 2 m (in which case only near-bottom samples were collected). Between 11 and 22 water samples were collected at each station during both deployments. During sampling the vessel was anchored between 7 and 15 meters away from each mooring and in-line with the surface current direction.

Water samples were transported back to the laboratory and filtered for SSC within 10 hours of collection, to minimize any change in the organic content of samples. Each water bottle was manually agitated, and aliquots of 100 mL to 200 mL were extracted and filtered through weighed, precombusted, Whatman GF/F filters with pore size of 0.7 µm. Loaded filters were dried at 50°C overnight and allowed to cool in a dessicator before weighing.

2.3 Analytical Methods

Tidal analysis of water level and depth-averaged along-channel velocity data was performed with T-tide software (Pawlowicz et al., 2002). T-tide could only find tidal constituents with periods of 15 days per cycle and shorter, due to the water level records from the instruments being less than 29 days. YSI profile raw data was manually edited as necessary to average together multiple returns from the same depth and to eliminate data from bottom hits and sensor saturation. The SSC data derived from filtering the water samples were used to calibrate the YSI turbidity from NTU to mg L^{-1} with a simple linear regression for each YSI. Water level data from the AWAC and the ADCP were corrected for post-deployment changes in barometric pressure using the inverse barometer method, and in the case of the AWAC, for a systematic pressure offset.

2.3.1 SSC estimation from Backscatter Intensity inversion

The SSC timeseries from the moored YSIs were used to calibrate the ADCP and the AWAC echo intensity to SSC using ADCP post-processing routines developed for Matlab at Ifremer (Tessier et al., 2008; Sahin et al., 2017). Separate calibrations were performed for each of the current profilers, and also separately for February and September.

The echo intensity output by the current profilers was converted to relative backscatter intensity with the sonar equation:

$$BI = RL - SL + 2TL - Cst, \tag{3}$$

where *RL* is the received reverberation level, *SL* is the source level, *2TL* is the two-way transmission loss, and *Cst* is a constant function of the total scattering cross-section and particle mass. The received level was calculated as:

$$RL = B + (EC - EC_0) * Kc, \tag{4}$$

where *B* is the noise level (70 dB µPa^{-1} for the ADCP workhorse sentinel and 82 dB µPa^{-1} for the Nortek AWAC), *EC* is the echo intensity output by the current profiler, EC_0 is the echo value in air (45 counts for the ADCP workhorse sentinel and 30 counts for the Nortek AWAC), and *Kc* is a conversion coefficient (0.42 dB count^{-1} for the ADCP workhorse sentinel and 0.4 dB count^{-1} for the Nortek AWAC). The two-way transmission loss was calculated as:

$$2TL = -20\log(R) + 2\alpha R, \tag{5}$$

where *R* is the range to the ensonified water volume and α is a sound absorption coefficient, $-20\log R$ is the transmission loss due to geometrical attenuation for spherical spreading, and $2\alpha R$ is transmission loss due to water attenuation.

For the moored current profilers, the backscatter intensity in the current profiler bin closest to the height of the moored YSI above bottom was regressed against the timeseries of calibrated SSC from the moored YSI at each site. For each current profiler, the final form of the regression equation between BI and SSC was:

$$10\log(SSC) = a * BI + b, \tag{6}$$

where *a* and *b* are regression coefficients and *SSC* is the suspended sediment concentration in mg L^{-1}. See Appendix 1 for the values of all constants.

2.3.2 Iterative method for ADCP calibration to SSC

The initial regression equations had very high amounts of scatter at both sites and both seasons (not shown), so the BI-SSC calibrations were redone using the implicit iterative method. In the implicit iterative method, a term describing the attenuation of the acoustic signal due to suspended sediment has to be added to Equation 3:

$$BI = RL - SL + 2TL - Cst + 2R\alpha_s, \tag{7}$$

where *R* is the along-beam distance and α_s is the sediment attenuation coefficient. This coefficient is calculated with the following set of equations (Thorne et al., 1991):

$$\alpha_s = \alpha_v + \alpha_d = 20\log\big(exp(1)\big)\,(\zeta_v + \zeta_d)SSC \tag{8}$$

$$\zeta_v = \frac{k(g-1)^2}{2\rho_s}\left(\frac{s}{s^2+(g+\theta)^2}\right) \tag{9}$$

$$\zeta_d = \frac{1}{2}\frac{\bar{\sigma}_{tot}}{\rho_s \bar{v}_s} \tag{10}$$

$$s = \frac{9}{4\beta}\left(1+\frac{1}{a_s}\right);\quad g = \frac{\rho_s}{\rho_0}\;;\quad \theta = \frac{1}{2}\left(1+\frac{9}{2\beta a_s}\right);\quad \beta = \sqrt{\frac{\omega}{2\upsilon}}\;;\quad \omega = 2\pi f;$$

where ζv is the viscous absorption of sound due to sediment, ζ_d is the scattering of sound by sediment, *f* is the frequency of the acoustic instrument, *k* is the acoustic wavenumber, ρ_0 is the density of water, ρ_s is the density of the sediment, υ is the kinematic viscosity of water, a_s is the sediment particle radius, and σ_{tot} is the global scattering cross-section of the sediment particles. The sediment attenuation coefficient cannot, however, be solved for and simply added to the equation because it depends on SSC (Equation 8), and the attenuation due to sediment in the bins closer to the ADCP affects the backscatter in the farther bins. It has to be found through an iterative approach for each ADCP bin in sequence (Thorne et al.,1991; Tessier et al. 2008).

The iterative method calculates the effective mean backscattering cross-section and the global scattering cross-section for particles of a single diameter. Different calculations are used for sand (Thorne et al. 1991) or flocculated particles (Thorne et al., 2014). Two output variables are used with the particle density to calculate the scattering index and the two sediment absorption parameters: viscous absorption and diffusive absorption.

After calculating these parameters, the iterative method starts with the ADCP bin closest to the instrument. It calculates an initial value for the total sediment absorption (*qs0*) and calculates the SSC from Equations 6 and 7, with fit parameters *a* and *b* equal to 1. It cycles through incrementing values of *qs0*, comparing the output SSC to the SSC at the previous iteration, and stops when the difference is below a pre-determined value (1 mg L^{-1}). It then moves up to the next highest ADCP bin, using the values of *qs0* in the underlying bin as the starting point for the new bin. The end result is a timeseries of SSC profiles without making an empirical regression.

One major flaw in this method is that any error in the lower ADCP bins will propagate up to the upper bins (Thorne and Hanes, 2002). Additionally, suspended fine sediment in estuaries is very likely to be flocculated and to contain more than one particle size. The original implicit method was thus judged to be unsuitable for the present study. One addition was therefore made to the original iterative method to improve the accuracy of the resulting SSC timeseries.

2.3.3 Optimal diameter

Because a major weakness of the iterative method is the assigned particle size, the theoretical optimal diameter (*Dopt*) necessary to generate accurate SSCs was calculated. The method was based on work done by Cron (2012), and consists of a modification to the implicit iterative method equations. The improved equations loop through a series of specified particle diameters, calculating SSC via the iterative method for each diameter from 1 to 1000 µm and saving the results for Bin 3 after each iteration. Bin 3 was used because the YSI was moored at a height above bottom corresponding to this ADCP bin. The resulting Bin 3 SSCs can then be compared to the YSI SSC, and the optimal diameter at each timestep is the diameter that generated the smallest difference between SSCs. Assuming the optimal diameter is constant with depth, the resulting timeseries of optimal diameter can then be used in the regular iterative method to calculate SSC profiles with sediment attenuation.

Using optimal diameters with the implicit iterative method corrected the Backscatter Intensity, and decreased the amount of scatter in the final relationships between Backscatter Intensity and the SSC measured by the moored YSIs (Figure 2). The SSC generated by the iterative method was also compared with the SSC measured by the profiling YSI (Figure 3, Table 2). The scatter in the figure, the low r^2 values, and high root mean square error (RMSE) can be explained by the field methods. YSI profiles were collected while the boat was anchored within 10 m of each current profiler, and the boat drifted around this position with the tide. The resulting distances between YSI profile and current profiler combined with the turbulence and variability of the flow meant that the instruments were not measuring exactly the same subset of particles. This caused the relationship between YSI and current profiler SSC to be lower than it otherwise would if the distance between instruments could have been closer. Nevertheless, the relationship between the SSCs is positive, consistent with the variability between sites and seasons, and acceptable given the circumstances.

2.3.4 Suspended sediment flux

Suspended sediment flux was calculated from the ADCP/AWAC velocity, depth, and calibrated SSC. Along-channel velocity was calculated from the east and north velocity components output by the current profilers. The predominant current direction was determined from a histogram of near-surface current direction for Site 1, and from the compass orientation of the channel at Site 3. Two different methods were used because the AWAC determines a timeseries of near-surface current direction and the ADCP does not. Data in the current profiler bin containing the water surface was discarded. Reflection of the acoustic signal from the water surface can cause SSC to erroneously increase in the uppermost bins. Surface reflections were corrected by extrapolating to overlying cells the SSC value from the uppermost valid cell. Velocity and SSC for the water column below the lowermost current profiler bin were not interpolated, leaving SSC and velocity from the bottom 1.5 m of the water column unmeasured and not included in these calculations and analyses. Near-bottom SSC is generally higher than in the lowest current profiler bin, and near-bottom velocity is very low and decreasing toward zero. All sediment fluxes calculated could therefore be lower than they should be but in the correct directions.

Instantaneous Simple Flux was calculated according to Equation 1, and also depth-integrated for the portion of the water column above the bottom of the first ADCP bin. The Dyer Flux components (F1 through F7) were calculated according to Equation 2. Tidal cycle averaging (overbars, e.g. $\overline{C_t U_t H_t}$) was performed with a frequency-domain lowpass filter with a cutoff frequency of 36 hr^{-1}. The deviation components (subscript ‘t’. e.g. U_t) were calculated by subtracting the lowpassed datasets from the unfiltered datasets.

The fluxes reported and analyzed in this paper have a degree of uncertainty due to errors and uncertainties in the measurement of velocity and SSC, and in the calibration of the YSI and the inversion of the ADCP data. Uncertainty in velocity measurements is provided by the instrument manufacturers: the AWAC at Site 1 has a velocity accuracy of 1% of the measured value, and the ADCP at Site 3 has a velocity accuracy of 0.3% of the measured value. To calculate the error of SSC, the SSC in the water samples was compared to the final SSC derived by the implicit iterative method at the same time and depth that the water samples were taken. Mean Absolute Error between the water samples and ADCP SSC was calculated, and reported as the percent of the mean SSC of the water samples. There is a different error for each Site and Season, as summarized in Table 3. Flux uncertainty ranges between 25% and 47%.

2.3.5 Residual flux analytical model

To calculate residual flux components according to the Yu et al. (2012) model, the timeseries of water level, depth-average velocity, and depth-average SSC were first divided into tidal cycles. Model equations were fit to the time series data from each tidal cycle. All fitting was performed using a nonlinear least squares method, and the tidal cycle end points were determined from depth averaged velocity, starting with the first flooding velocity. Water level and velocity are fit to an equation including the M2 and M4 tidal frequencies:

$$U = u_0 + u_1 \cos(\omega t + \varphi_{u1}) + u_2 \cos(2\omega t + \varphi_{u2}) \text{ and} \tag{11}$$

$$H = h_0 + h_1 \cos(\omega t + \varphi_{h1}) + h_2 \cos(2\omega t + \varphi_{h2}) \text{ ,} \tag{12}$$

where u_0 and h_0 are the tidal cycle means of velocity and depth respectively, u_1 and h_1 are the M2 amplitudes, u_2 and h_2 are the M4 amplitudes, ω is the M2 angular frequency, ψ_{u1} and ψ_{h1} are the M2 tidal phases, and ψ_{u2} and ψ_{h2} are the M4 tidal phases. Three other variables are calculated:

$$\hat{u}_0 = {}^{u_0}/_{u_1} \tag{13}$$

$$\hat{u}_2 = {}^{u_2}/_{u_1} \tag{14}$$

$$\hat{h} = {}^{h_1}/_{h_0} \tag{15}$$

The model for depth-average SSC is more complicated, and involves many of the fitted amplitudes and phases in Equations 11-15 and three additional coefficients to fit.

$$C = \sum_{i=1}^{8} E_i = \sum_{i=1}^{8} \frac{A_i}{\sqrt{\left(\omega_i^2 + D^2\right)}} \cos(\omega_i t + \gamma_i + \theta_i)$$

$$\theta_i = \tan^{-1}\frac{\omega_i}{D} \qquad (16)$$

The eight E_i terms each have a particular equation for A_i, ω_i, and γ_i according to Table 4. *D*, *B*, and *k* in the Appendix are terms to be fitted. *D* represents the deposition potential, *B* the resuspension potential, and *k* the along-channel SSC gradient.

After fitting water level, velocity, and SSC to equations 11-16, the flux components F1 through F5 can be calculated as follows:

$$F1 = \frac{u_1^3 h_0}{D}\left(\frac{1}{2}\frac{B}{h_0}\hat{u}_0 - \frac{k}{u_1}\hat{u}_0^2\right) \qquad (17)$$

$$F2 = \frac{u_1^3 h_0}{2D}\cos(\varphi_{u1} - \varphi_{h1})\left(\frac{1}{2}\frac{B}{h_0}\hat{h} - \frac{k}{u_1}\hat{u}_0\hat{h}\right) \qquad (18)$$

$$F3 = -\frac{u_1^3 h_0}{2\sqrt{\omega^2+D^2}}\left(\frac{k}{u_1}\hat{u}_0\hat{h}\right)\cos(\varphi_{u1} - \varphi_{h1} - \theta_\omega) \qquad (19)$$

$$F4 = \frac{u_1^3 h_0}{2\sqrt{\omega^2+D^2}}\left[\left(-\frac{k}{u_1} + 2\frac{B}{h_0}\hat{u}_0 - \frac{1}{2}\frac{B}{h_0}\hat{h}\cos(\varphi_{h1} - \varphi_{u1})\right)\cos\theta_\omega + \frac{B}{h_0}\hat{u}_2\cos(2\varphi_{u1} - \varphi_{u2} - \theta_\omega) - \frac{1}{4}\frac{B}{h_0}\hat{h}\cos(\varphi_{h1} - \varphi_{u1} - \theta_\omega)\right] + \frac{u_1^3 h_0}{2\sqrt{4\omega^2+D^2}}\left[-\frac{k}{u_1}\hat{u}_2^2 cos\theta_{2\omega} + \frac{1}{2}\frac{B}{h_0}\hat{u}_2\cos(2\varphi_{u1} - \varphi_{u2} - \theta_{2\omega})\right] \quad (20)$$

$$F5 = \frac{u_1^3 h_0}{8\sqrt{4\omega^2+D^2}}\frac{B}{h_0}\hat{h}\cos(\varphi_{u1} - \varphi_{h1} - \theta_{2\omega}) - \frac{u_1^3 h_0}{4\sqrt{\omega^2+D^2}}\frac{k}{u_1}\hat{u}_2\hat{h}\cos(\varphi_{u1} - \varphi_{u2} + \varphi_{h1} - \theta_\omega) \quad (21)$$

where $\theta_\omega = \tan^{-1}\frac{\omega}{D}$ and $\theta_{2\omega} = \tan^{-1}\frac{2\omega}{D}$.

The flux components F1 through F5 as calculated by the Yu model correspond to the Dyer Fluxes of the same designations (so Yu F1 is the same residual flux component as Dyer F1). The Yu model does not calculate the vertical components, F6 and F7. The eight E terms are meaningful as well, but they were not analyzed for the present paper. The Yu model results are in discrete data points, one per tidal cycle, instead of continuous timeseries.

To better compare the Yu Fluxes to the Dyer Fluxes, depth-averaged timeseries were calculated for the Dyer components F1 through F5. After depth-averaging, the Dyer Fluxes were averaged according to the same tidal cycle end points used in the Yu model calculations. The relative error between the two methods for each tidal cycle was calculated (as Dyer – Yu)/Dyer), and a Wilcoxon ranked sum test (alpha = 0.05) was performed for each flux component. The null hypothesis for the Wilcoxon test was that there is no difference between the two flux method results.

3. Results

Data collected for this project comprises downloaded datasets of weather and river discharge, with experimental measurements of water level, velocity, and SSC. These results and the Dyer Fluxes will be presented by season in Sections 3.1 and 3.2. Yu Fluxes will be summarized in Section 3.3.

3.1 February: high river discharge

3.1.1 Discharge, weather, water levels

River discharge measured above the head of tides at Châteaulin was 86.3 $m^3 s^{-1}$ on the first day of deployment. The discharge increased to a high of 95 $m^3 s^{-1}$ on 11 February, and then steadily decreased throughout the deployment to 20.8 $m^3 s^{-1}$ (Figure 4A). Weather conditions varied during the deployment period (Figure 4B-F). The first week of the deployment was characterized by frequent rain at Brest. Wind directions were initially westerly to northerly, but became predominantly easterly after the first week. Barometric pressure varied between 1030 and 992 mbar. Wind speed varied up to 8 $m s^{-1}$ throughout the deployment period.

Water level data was analyzed from the two moored current profilers (Figure 5) and from the gauging station at Guily-Glaz (not shown) during the February deployment. Water levels on the Aulne were semidiurnal with a very slight diurnal inequality and pronounced spring-neap variability. Site 1 had a spring tide range of 6.9 m and neap tide range of 2 m, with an almost symmetrical tide. The tide at Site 3 had a shorter flooding phase and a longer low tide phase relative to Site 1. The spring tide range at Site 3 was 6.5 m and the neap tide range was 2 m. At Guily-Glaz (not shown) the flooding tide was considerably shorter than the ebbing phase, and low tide was lengthened to a duration of over 2 hours. The spring tide range was 4.3 m and the neap tide range was 1.85 m.

The principle lunar semidiurnal tidal component (M2) decreased with distance landward and the M4 overtide component increased with distance landward (Table 5). Relative distortion, or the ratio of M4 to M2 amplitude, also increased landward, with most of the increase in distortion occurring between Site 3 and Guily-Glaz. The phase difference at all three sites was less than 180 degrees, indicating flood dominance.

3.1.2 Velocity and SSC

Velocity at Site 1 was strongest during ebbing and during spring tide, with a near-surface maximum in the top 2 to 4 m (Figure 5A). Maximum flooding velocities during spring tides were between 0.84 and 0.73 m s^{-1}, and maximum ebbing velocities between -0.81 and-0.87 m s^{-1}. Neap tide velocities were lower by 0.2 – 0.4 m s^{-1} (Figure 6A). Velocity was slightly ebb dominant, and the slack periods after high and low tide were roughly equal in duration.

The highest SSC values at Site 1 were in February during spring tides. Flooding usually featured two pulses of increased SSC, normally less than 80 mg L^{-1}, with the mid-flood pulse being higher (Figure 5B). Ebbing SSC was characterized by a near-surface maximum about 20 mg L^{-1} more concentrated than the underlying water. Neap tide concentrations were much lower, generally less than 25 mg L^{-1}, with the exception of a spike in SSC on February 21 (Figure 6B).

Velocity at Site 3 had a pronounced distortion in February, with strongest flooding and ebbing velocities both occurring within 1 hour of low tide (Figure 5C). Maximum flooding velocities were between 1.4 and 1.5 m s^{-1}, and maximum ebbing between -1.2 and -1.6 m s^{-1} (Figure 7A). Ebbing velocity was also characterized by strong shear, with surface velocity 0.5 to 0.8 m s^{-1} higher than velocity at the bottom in February. The slack period after low tide lasted 15 to 30 minutes, but the slack after flooding persisted for about 3 hours.

SSC at Site 3 in February was highest during spring tide flooding, with maximum values in the lowest 1 meter above the ADCP (Figure 5D). The highest SSC occurred within 1 hour of low tide, during times of strongest velocity. Maximum spring tide concentrations during February were as high as 2 g L^{-1} with neap tide concentrations much lower, below 150 mg L^{-1} (Figure 7B).

3.1.3 Dyer Fluxes

The directions of depth-averaged residual sediment fluxes were mixed at Site 1 in February (Figure 6). The F1 Eulerian flux from longer-than-tidal processes was seaward during spring tides, and slightly landward, up to 1.06 g m^{-1} s^{-1}, during neap tides. The F2 flux due to Stokes drift was much lower in magnitude and slightly landward. F2 was predominantly landward up to 5.22 g m^{-1} s^{-1}, but became slightly seaward up to -0.10 g m^{-1} s^{-1} during neap tide. The three tidal pumping components were of much lower magnitude than the F1 advective component, but comparable to the F2 component. F4 was about 1 order of magnitude greater than F3 and F5, varying between 17.16 g m^{-1} s^{-1} landward and -14.44 g m^{-1} s^{-1} seaward. The F4 flux was predominantly landward during spring tides and seaward during neap, but in both cases occasionally decreased close to zero. The F3 tidal pumping component was predominantly landward during the first spring tide by up to 1.57 g m^{-1} s^{-1} but was seaward by -0.56 g m^{-1} s^{-1} during neap tide. The F5 component was similar to F3, but was stronger on the first spring tide, up to 3.03 g m^{-1} s^{-1}. Neap tide F5 flux varied around zero between 0.67 and -0.63 g m^{-1} s^{-1}. The vertical components F6 and F7 were very minor in magnitude, very slightly seaward, and had no spring/neap variability.

The total residual Simple Flux at Site 1 was strongly dominated by the F1 component and modulated by the F4 component. The contributions of the other components were minor by comparison. The total residual Simple Flux was up to -28.0 g m^{-1} s^{-1} seaward during the first spring tide, and predominantly seaward between 1.85 and -16.13 g m^{-1} s^{-1} during neap tide. The cumulative total depth-averaged residual Simple Flux during the deployment was 13.58 x10^3 kg $m^{-1}s^{-1}$ in the seaward direction (Figure 6F).

Residual fluxes at Site 3 were very different from those at Site 1 (Figure 7). The F1 Eulerian flux was the strongest component of advective flux, but it was almost completely opposed in magnitude and direction by the F2 Stokes drift flux. The F1 flux was seaward by up to -321.4 g m^{-1} s^{-1} during the first spring tide and -470.3 g m^{-1} s^{-1} during the second. By contrast the F2 flux was up to 215.5 g m^{-1} s^{-1} landward during the first spring tide and 361.4 g m^{-1} s^{-1} during the second. During neap tide, the F1 flux decreased markedly to -5.5 to -0.8 g m^{-1} s^{-1} seaward, and the F2 flux to 1.3 to 3.1 g m^{-1} s^{-1} landward.

As at Site 1, the F4 term was the strongest of the three tidal pumping components. Unlike at Site 1, however, the tidal pumping components were much closer in magnitude to the F1 advective component. F3 was landward during spring tides. F4 flux was seaward during the first spring but became landward during the second. F5 was landward spring tides. All three tidal pumping terms decreased dramatically and changed direction repeatedly during neap tide. The vertical components F6 and F7 were close in magnitude to the terms F3 through F5. Unlike at Site 1, the vertical terms were stronger during spring tides than at neap tides, and seaward.

The total residual Simple Flux was up to -104.7 g m^{-1} s^{-1} seaward during the first spring tide but landward by up to 380.2 g m^{-1} s^{-1} during the second. The total Simple Flux was influenced strongly by the direction of the F4 term, with the change in direction during the second spring tide driving the total Simple Flux landward. The cumulative total residual Simple Flux during the deployment was seaward through the first spring tide and neap tide, but the stronger landward F4 flux during the second spring tide drove the cumulative total Simple Flux landward, and the three-week deployment period ended with a cumulative total Simple flux of 167.3 x10^3 kg m^{-1} in the landward direction (Figure 7F).

3.2 September: low river discharge

3.2.1 Discharge, weather, water levels

River discharge measured above the head of tides at Châteaulin was between 1.32 and 3.67 m^3 s^{-1} during the deployment (Figure 8A), with lowest values on 3 September and rising to a peak on 18 September. Weather conditions varied slightly during the deployment period (Figure 8B-F). Wind speed varied between 0 and 10 m s^{-1} and a diurnal variability, with highest wind speeds generally in the evening. Winds were predominantly from the north to northwest, with easterly to northeasterly winds in the first three days and easterly to southerly winds in the last two. Atmospheric pressure was 1006 mbar to 1032 mbar. There was some precipitation on most days during the deployment, but no more than 6 mm in any given 6-hour period and never all day.

3.2.2 Velocity and SSC

Velocity at Site 1 in September was characterized by a mid-depth maximum during flooding and a near-surface maximum during ebbing (Figure 5E). As in February, maximum tidal velocities during spring tides were between 0.84 and -0.87 m s^{-1}, and neap tide velocities were lower by 0.2 – 0.4 m s^{-1} (Figure 9A). Velocity was slightly ebb dominant, and the slack periods after high and low tide were roughly equal in duration.

During September, SSC at Site 1 was highest near bottom and during spring tides (Figure 5F). SSC was highest during mid-ebb and lowest during high tide, with moderately increased SSC during mid-flood. Spring tide SSC was roughly two to three times greater than neap tide (Figure 9B). SSC was mostly below 30 mg L^{-1} throughout the deployment, with neap tide values less than 15 mg L^{-1}.

Velocity at Site 3 had a pronounced distortion in September, with strongest flooding and ebbing velocities both occurring within 1 hour of low tide (Figure 5G). As in February, maximum tidal velocities were close to 1.5 and -1.6 m s^{-1} (Figure 10A). Ebbing velocity was characterized by strong shear, with surface velocity 0.3 m s^{-1} higher than velocity at the bottom in September. The slack period after low tide lasted 15 to 30 minutes, but the slack after flooding persisted for about 3 hours.

SSC at Site 3 in September was highest during the periods of strongest velocity, within 1 hour of low tide (Figure 5H). The periods of high SSC were limited in duration, with maxima most often below 150 mg L^{-1} and values less than 30 mg L^{-1} for most of the tidal cycle (Figure 10B).

3.2.3 Dyer Fluxes

Depth-averaged residual suspended sediment fluxes at Site 1 were much lower in magnitude in September than in February, and there were important differences in the variability of some of the flux components (Figures 9). The F1 Eulerian flux was seaward throughout the deployment by -0.67 to -3.79 g m^{-1} s^{-1}. The F2 Stokes drift flux was landward throughout the deployment, but on the same order of magnitude as F1. The F4 flux was the strongest component of tidal pumping flux, but the sign during spring and neap tides was reversed from February. F4 was seaward during spring tides and seaward but close to zero during neaps. The F5 flux was predominantly landward during spring tides, up to 0.62 g m^{-1} s^{-1}, and between 0.08 and -0.04 g m^{-1} s^{-1} during neap tide. The F3 component was much weaker than the other flux components, and varied between 0.01 g m^{-1} s^{-1} landward and -0.04 g m^{-1} s^{-1} seaward with little spring/neap variability. The vertical components F6 and F7 were much smaller in magnitude than the other components. F6 was slightly landward and F7 was slightly seaward. Neither had appreciable spring/neap variability.

The total Simple Flux was controlled by a combination of F1 and F4 fluxes and was seaward throughout the deployment with no spring/neap variability. The total Simple Flux varied between 0.32 and -5.69 g m^{-1} s^{-1}. The cumulative total Simple Flux was seaward throughout the deployment period, and ended with a value of -3.14×10^3 kg m^{-1} (Figure 9F).

Residual sediment fluxes at Site 3 were roughly similar to fluxes calculated for February, differing mainly by being lower in magnitude (Figure 10). The F1 and F2 advective components opposite each other in sign, but close to equal in magnitude. The F1 Eulerian flux was seaward during spring tide by up to -15.54 g m^{-1} s^{-1}. During neap tides it was close to zero, and slightly landward at times (-0.70 to 0.53 g m^{-1} s^{-1}). The F2 Stokes drift flux was landward throughout the deployment, but close to zero during neap tide. The tidal pumping components were of lower magnitude than the advective components. F3 and

F5 were landward during spring tides and slightly seaward during neaps, but F4 was opposite in direction. F3 was landward by 4.5 to 7.5 g m^{-1} s^{-1} during spring tide, but close to zero during neap tide. F4 was seaward -16.4 to -17.5 g m^{-1} s^{-1} during spring tide, and slightly landward during neap tide. The F5 component was landward during spring tides, and slightly seaward during neaps. The vertical components F6 and F7 were less than the terms F3 through F5, but up to six times stronger than at Site 1. Unlike at Site 1, the vertical terms were stronger during spring tides than at neap tides, and seaward. Total flux was landward during spring tides and zero to slightly seaward during neaps, with a total range of variability of -0.70 to 11.75 g m^{-1} s^{-1}. The cumulative total Simple Flux was landward throughout the deployment period, and ended with a value of 8.37 x 10^3 kg m^{-1} landward (Figure 10F).

3.3 Yu Fluxes

The calculated values for Dyer Fluxes and the Yu model Fluxes were closest during neap tides and for the advective components F1 and F2 (Figure 11). The difference between methods was greater at Site 3 than at Site 1 in both February and September. For the F1 advective flux, the Yu and Dyer methods were very similar during both spring tide and neap tide, and for both Sites and seasons. The datapoints all fell along a 1:1 line with relatively low scatter compared to the other flux terms. The F2 advective term (Stokes drift on the tide) was similarly close between flux methods. Much greater variability between flux methods was seen in the tidal pumping terms F3, F4, and F5. The relationship between Yu flux and Dyer flux for the F3 term was negative, and most of the problem occurred during spring tide and for Site 3 in February. Site 3 in September and Site 1 February and September were along the 1:1 line and had low scatter. The F4 flux was more similar between the Yu and Dyer methods, but the amount of scatter was greater. Like the F3 term, the F5 term had a negative relationship between the Yu flux and the Dyer flux. Datapoints for both the F4 and F5 terms had greater scatter overall, including Site 1 February and September, and Site 3 in September. In summary, the difference between methods was much smaller for the advective components than the tidal pumping components when taking the average of all tidal cycles together.

Although the difference between methods was minimal for most flux components on average, the relative error between methods for individual tidal cycles was highly variable. For flux components F1 and F2, relative error was predominantly within ±10% during spring tides in February. During the low-discharge month of September, the F1 and F2 relative error during spring tide was a little higher, varying up to ±42%. For both sites and both seasons the relative errors for flux components F3, F4, and F5 were as high was several hundred percent, with a very wide range of variability between individual tidal cycles. The difference between methods was also smaller at Site 1 near the mouth of the estuary and larger and more variable at Site 3. For both Sites, both seasons, and all flux components, the relative error during neap tides was much higher, many times exceeding 100% during individual tidal cycles.

The statistical similarity between the two flux methods was tested with a Wilcoxon signed rank sum test, with spring and neap tides tested separately (Table 6). The null hypothesis of no difference between methods was rejected for the F5 term most often. It was rejected at Sites 1 and 3 in February and September for spring tide, and Sites 1 and 3 in September during neap tide. At Site 3 the null hypothesis was rejected for F3 during February spring tide, and F3 and F4 during September spring tides. The null hypothesis could not be rejected at the 5% significance level for most of the flux terms in all four datasets. Similar to the visual interpretation of the plotted tidal cycle averages (Figure 11), the Yu model generates tidal cycle average fluxes that are not statistically different from the Dyer Flux components when considered over an entire spring-neap cycle, although results for individual tidal cycles can be highly variable.

4. Discussion

4.1 Sediment transport processes in the Aulne

In general, sediment transport in the Aulne River estuary is driven by tidal resuspension and modified by river discharge. Variability within tidal cycles and between spring and neap tides is a prominent feature of the system. Similarities in processes across the whole estuary are accompanied by distinct differences at the mouth and mid-estuary locations, as well as seasonal variability. In this section, the results will be interpreted for winter season high flow conditions and summer season low flow conditions.

4.1.1 High flow conditions

High flow conditions are represented by the February datasets. The tide range decreased very little from the mouth to the mid-estuary site (about 0.5 m on average), even though the mean water depth decreased from 19 m at the center of the channel at Site 1 to 5 m at Site 3. The result was an increase in the relative shallowness of the estuary in the landward direction, and hydrodynamic changes consistent with shallow estuary theory (Dronkers, 1986; Friedrichs and Aubrey, 1988). In particular, the horizontal tide became highly distorted and asymmetrical at the landward location. The velocity asymmetry was accompanied by extreme asymmetries in the durations of slack periods, ebbing, and flooding. These distortions of the tidal flow had a very strong effect on residual suspended sediment flux within the estuary.

At Site 1 the horizontal tide was slightly flood dominant with no apparent slack period asymmetry. SSC was low, and strongly controlled by tidal resuspension and settling rather than advection from elsewhere. The total residual depth-integrated suspended sediment flux was seaward during spring tide and lower to slightly landward during neap tide. The total flux was dominated by the F1 advective flux component, and the other components were minor by comparison.

Site 3 was very different from Site 1. The channel was much shallower, about half the depth of the Site 1 location. The tide range, however, was only about 0.5 m less on average, resulting in a relative shallowness (tidal amplitude divided by mean depth) of about 0.65 during spring tide (versus 0.18 at Site 1). The horizontal tide was highly distorted. Tidal velocity was strongly ebb dominant and the slack after ebb was reduced to 15 to 30 minutes. The flooding period was marked by lower velocities and a much longer duration, and the slack after flooding was extended in length as well. SSC was as high as 2 g L^{-1} at times, with highest values during the strongest tidal velocities. SSC was therefore highest immediately before and after the very short slack after ebb. SSC decreased to less than 150 mg L^{-1} during slack periods, even the short slack after ebb, most likely due to settling of suspended sediments. The flooding velocity pulse would have resuspended any sediment that settled during the slack after ebb, making large amounts of sediment available for landward transport. These characteristics at Site 3 combined to have a drastic effect on residual suspended sediment flux.

Although the velocity was stronger in the ebbing direction at Site 3, the total residual depth-integrated suspended sediment flux was landward (Figure 7). Total flux was slightly landward during the first spring tide and neap tide, and strongly landward during the second spring tide. A longer deployment would be necessary to determine which spring tide represents the most common condition, but note that river discharge was reduced by more than half between the first and second spring tides. The very long slack period after flooding, combined with the high SSC during flooding, allows much more time for suspended sediment to settle after flooding. By contrast, the very short slack after ebb and high velocity before and after it, restricts the time available for sediment to settle and prevents it from consolidating. The end result is an environment that favors landward sediment transport even though velocity is ebb dominant.

The total flux at Site 3 was not dominated by any one component. Rather, the first 5 components were all surprisingly similar in magnitude, and combined to make a landward total flux.

The F1 advective component is usually the strongest component, as seen at Site 1, and can be thought of as primarily a function of freshwater discharge, even though other longer-than-tidal processes like storms and groundwater discharge can affect it as well. At Site 3, however, the F2 Stokes drift component was about equal in magnitude but opposite in direction. Stokes drift on either waves or tides is controlled most strongly by the wave height, so the very small decrease in tide height with distance landward allowed the F2 component to increase in importance until it could fully oppose the F1 flux. Also note that all three tidal pumping components (F3, F4, and F5) are also much closer in magnitude to the advective components than they were at Site 1. This is due to the increased relative shallowness at Site 3 allowed the development of compound tides and overtides (such as M8, 2SM6, and SK3), which would affect the tidal pumping terms instead of the advective or vertical flux terms. The vertical flux terms (F6 and F7) were minor by comparison to the rest of the components.

4.1.2 Low flow conditions

Low-flow conditions were represented by the September deployment. The most prominent differences between low-flow and high-flow conditions are the river discharge and SSC. River discharge was 2 - 4 $m^3 s^{-1}$, rather than February's river discharge of 85 - 100 $m^3 s^{-1}$ in the first week of the deployment. Such low discharge values are typical of the Aulne, as is much lower amount of precipitation in July and August. SSC in September was lower by an order of magnitude at both Sites compared to February. SSC in the system does respond strongly to tidal resuspension and settling, but that is not sufficient to explain seasonal differences in SSC. Decreased river discharge ought to allow tidal effects to become more dominant in the estuary. Resuspension of sediments would therefore be expected to increase under increased tidal velocity. Seasonal SSC variability is more likely to be connected to river discharge by rainfall runoff, as the study area has much lower rainfall in summer than winter and a predominantly agricultural watershed. Under this scenario, the lower summer SSC would be caused by lower amounts of terrestrial sediment entering the watershed during this dry season.

Water levels were slightly lower than in February, but variability in instrument placement could have caused an apparent but false water level decrease. Apparent seasonal differences in water level at Site 1 were due to the steep bottom slope in the vicinity of the AWAC. Precision in instrument placement between deployments was less than the variability of the slope. The instrument could not be placed in the deepest part of the channel due to local regulations and permitting requirements.

The tide ranges in September were similar to February, as was the decrease in tide range between Sites 1 and 3 and the increase in relative shallowness. Tidal velocity was slower at both Sites. At Site 1, the near-surface peak in flooding velocity was replaced by a mid-depth peak. At Site 3 the tidal velocity was slower, but the extreme distortion seen in February was also present in September. Tidal velocity is potentially affected by several factors: water depth, friction with the bottom, and the amount of inundated channel area. The Aulne near Sites 1 and 3 does not flood much salt marsh or mudflat, and the channel width changes little between spring and neap tides compared to other sections of the river with salt marsh and mudflat areas. Shallower water in September due to lower precipitation and river discharge would cause friction with the bottom to affect a larger percentage of the water column, thus decreasing tidal velocities. The effect is more pronounced at Site 3 because it is shallower in general.

As a result of decreased velocity and SSC, residual suspended sediment fluxes were also lower in magnitude during low flow conditions at both Sites. Additionally, at Site 1 the F1 and Total fluxes lost their spring-neap variability. The presence or absence of spring-neap variability for the other flux components was consistent between February and September. At Site 3, all flux components retained their spring-neap variability, but the amount of variability was lower. The direction of cumulative residual depth-integrated flux was the same as in February, but the magnitudes were much lower.

The relationship between Backscatter Intensity and SSC was different between February and September. Physical properties of particles, such as presence or absence of flocculation, the size and shape of flocs or primary particles, and the particle/floc density or water content can affect the way that sound scatters from and travels through particles. Given that the same instruments were used at the same sites in both seasons, differences in the BI-SSC relationship must be caused by the particles and not the sound sources. Unpublished data from a LISST 100X laser particle size instrument indicates that the suspended particles were flocculated, and that floc size varied on tidal and fortnightly timescales (Moskalski et al., 2014). Furthermore, the floc sizes were larger at the mid-estuary site (Site 3) than at the mouth. Flocs behave differently in the water than solid particles of the same mass or size, so differences in floc size could contribute to seasonal differences in SSC and suspended sediment flux.

4.2 Implications of the Yu model

The Yu et al. (2012) simplified model of residual depth-averaged sediment flux yielded some important insights into the processes that control residual sediment flux in the Aulne. The Yu et al. (2012) method calculates residual horizontal suspended sediment fluxes based on a simplified model of five forcing mechanisms: the mean water depth; M2 horizontal tidal amplitude; residual, M2, and M4 velocities; and the depth-averaged SSC gradient. The Dyer Fluxes, on the other hand, are calculated on the observed dataset and include by default the full variability on all frequencies by all contributing mechanisms. Differences between the two methods therefore can be attributed to the influence of forcing mechanisms that are not included in the Yu et al. (2012) model.

Differences between the Yu and Dyer fluxes are greatest for Site 3 in February, greater during spring tide than during neap tide, and greater for the tidal pumping components than for the advective components. These differences between Dyer and Yu methods can be explained by the results of the tidal distortion and the variability of SSC in the Aulne.

Tidal analysis results on water level and along-channel velocity reveals the presence of M6 and M8 tidal harmonics, as well as some compound constituents such as 2SM6 and SK3. Several of these higher-frequency components have signal-to-noise ratios (SNR) greater than 1 at both sites in February, indicating that they are relatively important to the water level and velocity variability. The O1, K1, S2, and M3 constituents also have very high SNR. Even though the SNRs were below 1 for many of these components in September, these signals are nonetheless present in the water level and velocity data, and therefore could affect suspended sediment flux. Although the absence of these terms in the Yu model did not greatly affect the precision of the model's fit to depth-average velocity, it could be part of the reason why the fits to SSC were so poor.

The Yu model replicated observed water level very well and depth-averaged velocity reasonably well, but not SSC (Figure 12). R^2 for water level was consistently above 0.99, and for velocity it varied from 0.75 to above 0.99. For SSC, by contrast, the variation in r^2 values was extreme, being as low as 0.01 and as high as 0.94. These values were lowest for Site 3 in February (below 0.45), and mostly above 0.6 for Site 1. SSC is a critical component of suspended sediment flux, so difficulty in replicating SSC is more important than the higher-order tidal velocity constituents to the ability of the Yu model to replicate the Dyer Fluxes. Assumptions inherent to the Yu model appear to be of critical importance here.

The Yu model assumes that sediment flux occurs because of advection of a constant SSC gradient (Yu et al., 2012). A predictive equation is fit to the observations of depth-averaged SSC, with fitted parameters being the SSC gradient, a resuspension parameter, and a deposition coefficient. The fitted SSC gradient parameter varied, however, by three orders of magnitude and in sign among individual tidal cycles. Furthermore, the observed SSC gradient between Sites 1 and 3 in the Aulne varied hourly according to the spring/neap cycle (Figure 13). The turbidity maximum zone in the Aulne moves about 10 km in response to river discharge (Allen et al., 1980). This movement is part of the nonconstant SSC gradient. Given the strong spring/neap control of sediment resuspension and the mobility of the turbidity maximum zone, this simplification is not appropriate for the Aulne River estuary. Advection of the SSC gradient, deposition, and resuspension are not sufficient processes to model suspended sediment flux in the Aulne.

Although the Yu model does not explicitly include a fortnightly tidal term, the model did replicate the spring/neap variability in flux terms rather well. The fortnightly variability inherently present in the water level data is apparently sufficient to reproduce spring/neap flux variability in most cases. The dataset with the greatest difference in spring tide fluxes was Site 3 in February. Interestingly, Site 1 in February, which experienced the same river discharge conditions, had much smaller differences at spring tide. Site 3 in September, under low discharge conditions, also had smaller spring tide differences between methods. This leads us to believe that it is not the river discharge that is the cause of the larger differences between methods at spring tides. If this were the case, the relative differences should be similar at both sites under the same river discharge conditions.

4.3 Comparison to other studies

The Aulne River estuary has a consistently ebb dominant velocity and extreme asymmetries in tidal velocity and slack asymmetry. Tidal velocity and SSC are stronger during high-flow conditions and in the central estuary. Residual suspended sediment flux varies by location in the estuary and season, with stronger total flux and flux components in high-flow conditions and in the central estuary. At the mouth, the total residual flux is seaward, and controlled predominantly by the F1 advective flux. In the central estuary, the total residual flux is landward and driven by tidal pumping, because the F1 advective flux and the very strong F2 Stokes drift flux cancel each other out. This is similar to other estuaries in the literature, some of which are highlighted in this section.

Studies of two estuaries near New York City, USA contrasted high-flow and low-flow conditions. The microtidal Passaic River estuary in northern New Jersey has landward residual sediment flux during low discharge conditions, and seaward flux during moderate to high discharge conditions (Chant et al., 2011). During low discharge conditions the advective (F1, river discharge) component is weak relative to the tidal pumping flux (F4), whereas high discharge increases the magnitude of advective flux to the point that it is stronger than the tidal pumping flux. An anomalously weak spring freshet allowed the normally seaward residual flux in the microtidal Hudson River estuary to become landward during spring tides (Geyer et al., 2001). The unusual sediment flux direction was caused by a weaker than usual advective flux, which allowed the landward tidal pumping flux to dominate. In both cases the F1 Eulerian flux and F4 dispersive tidal pumping flux tend to be dominant during high-flow and low-flow conditions, respectively. These results are similar to the Aulne even though the estuaries are both microtidal and subject to a different hydrological regime.

The macrotidal Louisa Creek estuary in Australia is shallower and shorter than the Aulne, but its tides are similarly distorted (Lessa, 1996). Despite having a very similar tidal distortion, the sediment flux is landward only when the tide range is small. The Aulne, by contrast, has landward transport at Site 3 when the river discharge is low. The difference is due to the presence of wide intertidal mangrove forests in the Louisa Creek estuary. Whenever they are flooded, the ebb tide is strengthened and sediment flux becomes seaward. The sediment transport measured in Lessa (1996) was bedload flux, but the results are consistent with shallow tide theory (Friedrichs and Aubrey, 1998), and with the sediment flux in the Aulne.

Most sediment flux papers which decomposed the total residual flux calculated only the F1 and F4 terms, but some papers calculate more of the terms. Siegle et al. (2009) calculated all seven of the terms in the Dyer equation for a study in the shallow, microtidal Camboriú estuary in Brazil. This study was conducted during the rainy season, so freshwater discharge was high and the results should be compared to the February results in the Aulne. Although microtidal, the estuary is so shallow that the ratio of mean tide range to mean depth is similar to the Aulne at its mouth (about 0.4). They found that the tidal correlation (F4) and river discharge (F1) were the dominant flux components during spring tides. SSC was driven by tidal resuspension, as in the Aulne, making the F4 correlation component very high due to SSC increasing during strong velocities. The flux components due to vertical gravitational circulation (F6) and Stokes drift (F2) had secondary importance, but were about one quarter the magnitude of the F1 and F4 terms. Like in the Aulne, the Stokes drift component (F2) was landward while the F1 term was seaward. During neap tide, the F1 and F4 terms retained their dominance, and the F6 and F2 terms decreased in magnitude to the point of being individually negligible. Additionally, the F4 gravitational circulation term reversed direction during neap tide to become landward. Total residual suspended sediment flux was seaward during spring and neap tides.

Another Brazilian estuary, the Itajaí-Açu, was studied in a similar manner during low discharge conditions (Schettini et al., 2006). The Itajaí-Açu estuary is larger and deeper than the Camboriú, with a much lower tide range to mean depth ratio (0.1). It is also a highly stratified salt wedge estuary, so the following results are for the salt wedge portion of the estuary only and comparison to the Aulne will be made with Site 1 near the mouth. During spring tide the most important components for residual suspended sediment flux in the Itajaí-Açu were river discharge (F1, seaward), Stokes drift (F2, landward), tidal correlation (F4, landward), and gravitational circulation (F6, landward). In contrast to the Camboriú estuary (and the Aulne), the F6 term was the strongest contributor to the total residual flux, twice as strong as the F1 term. Furthermore, SSC in the Itajaí-Açu is not affected as much by resuspension, leading to the decreased importance of the F4 term relative to the Camboriú and the Aulne.

Similar to these Brazilian papers, Uncles et al. (1985) calculated the full complement of Dyer Flux terms for the Tamar estuary in England, and applied them to water, salt, and sediment. As at other estuaries, advective flux due primarily to freshwater discharge was consistently seaward, and tidal pumping dominated residual sediment flux during spring tides. Tidal pumping flux was landward in the upper and central estuary, but seaward closer to the mouth. Residual flux due to vertical shear was present, and usually directed landward, but it was minor by comparison to tidal pumping. Sediment flux was stronger during spring tides due to increased sediment resuspension from the bottom.

4.4 Estimating total residual flux

Most researchers (including the authors of this study) learned to calculate only some of the Dyer Flux terms when studying suspended sediment flux, usually the Eulerian and dispersive terms (F1 and F4). The other flux components are ignored as being minor contributors to the total residual flux in most cases (e.g. Sommerfield and Wong, 2011; Scully and Friedrichs, 2007; Kim and Voulgaris, 2008; Geyer et al., 2001; Gardner and Kjerfve, 2006). Although a common practice, it is worth asking if ignoring some of the flux components gives reasonably accurate results compared to instantaneous flux. Are the ignored terms truly minor, either alone or in combination, in every circumstance?

In order to address this question, we calculated Dyer Flux terms F6 and F7 according to Equation 2 and tried several combinations of all seven Dyer terms. In particular, the three combinations of most interest were F1 + F4 (Eulerian + dispersive), F1 through F5 (all horizontal terms), and F1 through F7 (including vertical components). These were compared to the depth-integrated, lowpass-filtered Instantaneous Simple Flux (Equation 1, Total Flux in the figures). The assumption herein is that the Simple Flux is the full correct answer, to which the Yu model and Dyer decomposition should be compared. The sum of the Yu Flux terms was also included in the comparison, as Total Yu Flux.

At Site 1 in February, all combinations of flux terms were negative (seaward), both instantaneously and cumulatively (Figure 14). The combination that came closest to the Instantaneous Simple Flux was F1 through F7, followed closely by F1 + F4. In non-cumulative mode, either of these two combinations would give similar results. Cumulatively, the addition of vertical terms causes an overprediction, while F1 + F4 underpredicts. Adding F1 through F5 underpredicted the cumulative Instantaneous Simple Flux. Total Yu Flux was the worst-performing, both in the non-cumulative and cumulative modes.

At Site 3 in February, the closest match to the cumulative Instantaneous flux was with adding F1 through F5 (Figure 15). In fact, it is so close that it cannot be distinguished from Instantaneous Simple Flux in Figure 15B, and can barely be distinguished in the non-cumulative part, Figure 15A. Adding F1 + F4 yielded a “total” flux that was seaward instead of the landward Instantaneous flux. Adding all seven components resulted in the correct direction but much lower magnitude, and a final cumulative value of only 43.9% of the Instantaneous Simple Flux value. Total Yu Flux yielded a result similar to F1 through F7.

In September at Site 1, adding only F1 and F4 yielded a cumulative flux that was higher in magnitude than the cumulative Instantaneous Simple Flux throughout the deployment period, and ended with a value that almost twice the cumulative Instantaneous Simple Flux value (Figure 16). Adding F1 through F5 resulted in a smaller overprediction, and adding the vertical flux terms did not improve the match. Total Yu Flux also overpredicted Instantaneous Simple Flux. In non-cumulative mode, both F1 through F7 and F1 through F5 yielded similar timeseries curves.

As in February, at Site 3 in September adding F1 through F5 yielded the closest match to the cumulative Instantaneous Simple Flux (Figure 17). Adding F1 and F4 yielded a “total” flux that was again the wrong direction. Adding all seven components resulted in a final cumulative value that was close to zero. The best match to cumulative Instantaneous Flux was adding F1 through F5. The Total Yu Flux slightly overpredicted the Instantaneous Simple Flux. In non-cumulative mode, F1 through F5 was so close to Instantaneous Simple Flux as to be indistinguishable on Figure 17A.

The common practice of using only the F1 and F4 components of the Dyer Flux equation to estimate “total” residual flux yielded an acceptably close value in only one of the deployments, Site 1

February. In all other datasets the best match required adding F1 through F5. Using only the F1 and F4 components yielded a "total" flux that was about twice the actual value at Site 1 in September, and in the wrong direction entirely at Site 3. The first 5 Dyer Flux components are all necessary to calculate in the Aulne.

The F2 Stokes drift flux proved to be critical at Site 3. The estuary becomes very shallow at that site, about 8 meters mean water level, but retains a 6.5 m spring tide range. The Stokes drift becomes much stronger than at the mouth as a result of this shallowing. Furthermore, the velocity distortion combined with strong tidal sediment resuspension generates stronger F3 and F5 components.

The vertical components F6 and F7 did not prove to be necessary for any of the datasets. F1 through F7 could be used at Site 1 in both seasons, but leaving them out would have made only a small difference in February and little difference in September. Vertical processes do contribute to flux near the mouth, but only in February and only to a minor extent. Vertical terms caused flux estimates at Site 3 to be underpredicted in both seasons. Site 3 is very shallow, yet retains a very large tide range. The mixing at this site is much stronger than at Site 1 (Moskalski et al., 2018) and the water column is much more well mixed, eliminating the vertical differences in water properties that drive vertical fluxes. Although vertical processes do exist in estuaries and they can contribute to residual flux, in the Aulne the effect is not strong enough to require calculating these terms or using them.

5. Conclusions

The goal of this study was to quantify the magnitude and direction of suspended sediment flux in a shallow, macrotidal estuary, and determine its most important forcing mechanisms, using the classic Dyer flux decomposition equation and a simplified analytical model. Several important conclusions can be summarized.

1. *The magnitude and direction of total residual suspended sediment flux change with position in the estuary and seasonally*. The total residual sediment flux is seaward near the mouth, and landward and greater in magnitude in the central part of the estuary. Fluxes are higher in February than September at both sites.
2. *The F1 Eulerian flux component is the dominant contributor to total residual flux at the mouth, but the tidal pumping components and the Stokes drift component increase in importance with distance landward*. The extreme distortion of tidal velocity with distance landward creates higher-order overtides and compound tides that are not included in the Yu et al. model. These higher-order tidal constituents are, nevertheless, expressed in the tidal pumping flux components F3, F4, and F5.
3. *The Yu model was unable to fit its SSC equations to observations of SSC with the same degree of accuracy as water level and velocity.* This was most likely due to a highly variable longitudinal SSC gradient instead of the constant one assumed by the model.
4. *The six processes included in the Yu et al. model are not sufficient to replicate individual flux components in the Aulne*. The mean water depth, the M2 horizontal tidal amplitude, the residual, M2, and M4 tidal velocities, and the depth-averaged SSC gradient were sufficient to replicate the F1 and F2 advective flux components, especially during spring tides. In contrast, the differences between methods for the tidal pumping components were much greater, and extremely variable between individual tidal cycles.
5. *The six processes included in the Yu et al. model did not consistently replicate the total residual Dyer Flux when the components were added.* The total Yu Flux was lower in magnitude than the Dyer Flux (both using F1 through F5) and the Simple Flux (Equation 1) for Site 1 in February, greater than both for September, and mixed for Site 3 February. The difference between Yu and Dyer was greater during spring tides than during neap, and greater in the central estuary than

near the mouth. The cumulative result of the instantaneous differences between the Yu model and the Simple Flux was underpredition of cumulative Simple Flux in February and overpredicting in September. Further research into the effects of higher-order tidal constituents and variable SSC gradient on suspended sediment flux are needed.

6. *All of the first five components of the Dyer flux decomposition equation were needed to accurately estimate the instantaneous flux in the Aulne River estuary.* Only one deployment could accurately use F1 plus F4 instead of all five components. The macrotidal and highly distorted nature of the tides made Stokes drift flux and the F3 and F5 tidal pumping terms critically important in the landward location. Our recommendation is that the first five Dyer Flux components definitely be calculated in all macrotidal and highly distorted estuaries. Calculating all of the Dyer Flux components should also be considered in microtidal and mesotidal estuaries if F1 plus F4 does not compare very strongly to the lowpass-filtered instantaneous Simple Flux.

The shallowing of the estuary landward combined with little decrease in tide range distorts the water level and velocity in the upper estuary, and creates a very complex hydro-sedimentary system in the Aulne. The forcing mechanisms contributing to residual suspended sediment flux in the Aulne estuary comprise overtide and compound tidal velocity constituents, and complex SSC variability in addition to those included in the Yu model (the mean water depth; M2 horizontal tidal amplitude; residual, M2, and M4 velocities; and the depth-averaged SSC gradient).

6. Data availability

Data are available upon request to the corresponding author, and they are also in the process of being uploaded to Mendeley Data.

7. Acknowledgements

We would like to thank our scientific divers, Erwan Amice, Thierry Le Bec, and Isabel Bihannic. We also thank our field helpers Guillaume Fromant, Véronique Cuq, Helen Piete, and Christophe Prunier.

Funding: This project received support from the state of France managed by the National Research Agency under the program “Investissements d’avenir” with the reference number ANR-10-LABX-19-01.

8. References

Acolas, M.L., V. Véron, H. Jourdan, M.L. Bégout, M.R. Sabatié, Baglinière, J.L., 2006. Upstream migration and reproductive patterns of a population of allis shad in a small river (L’Aulne, Brittany, France). ICES Journal of Marine Science 6, 476-484. doi 10.1016/j.icesjms.2005.05.022.

Allen, G.P., Salomon, J.C., Bassoullet, P., du Penhoat, Y., de Grandpré, C., 1980. Effects of tides on mixing and suspended sediment transport in macrotidal estuaries. Sedimentary Geology 26, 69-90.

Bassoullet, P., 1979. Etude de la dynamique des sediments en suspension dans l’estuaire de l’Aulne (Rade de Brest). PhD thesis : Université de Bretagne Occidentale.

Chant, R.J., Fugate, D., Garvey, E., 2011. The shaping of an estuarine Superfund site: Roles of evolving dynamics and geomorphology. Estuaries and Coasts 34, 90-105.

Cron, A., 2012. Quantification de la concentration en matières en suspension par méthode acoustique: Application à la dynamique sédimentaire en estuaire de Seine. Masters thesis: Université de Bretagne Occidentale.

Dronkers, J., 1986. Tidal asymmetry and estuarine morphology. Netherlands Journal of Sea Research 20, 117-131.

Dyer, K.R., 1997. Estuaries: A physical introduction, 2nd ed. John Wiley & Sons, New York.

French, J.R., Burningham, H., Benson, T., 2008. Tidal and meteorological forcing of suspended sediment flux in a muddy mesotidal estuary. Estuaries and Coasts 31, 843-859.

Friedrichs, C.T., Aubrey, D.G., 1988. Non-linear tidal distortion in shallow well-mixed estuaries: A synthesis. Estuarine, Coastal and Shelf Science 27, 521-545.

Friedrichs, C.T., Perry, J.E., 2001. Tidal salt marsh morphodynamics: A synthesis. Journal of Coastal Research SI 27, 7-37.

Gardner, L.R., Kjerfve, B., 2006. Tidal fluxes of nutrient sna dsuspended sediments at the North Inlet – Winyah Bay National Estuarine Research Reserve. Estuarine, Coastal and Shelf Science 70:681-692.

Geyer, W.R., Woodruff, J.D., Traykovski, P., 2001. Sediment transport and trapping in the Hudson River estuary. Estuaries 24, 670-679.

Grasso, F., Verney, R., Le Hir, P., Thouvenin, B., Schultz, E., Kervella, Y., Kohjasteh Pour Fard, I., Lemoine, J-P., Dumas, F., Garnier, V., 2018. Suspended sediment dunamics in the macrotidal Seine estuary (France): 1. Numerical modeling of turbidity maximum dynamics. Journal of Geophysical Research Oceans 123, 558-577.

Hansen, D.V., Rattray, M., 1966. New dimensions in estuary classification. Limnology and Oceanography 11, 319-326.

Kim, Y.H., Voulgaris, G., 2008. Lateral circulation and suspended sediment transport in a curved estuarine channel: Winyah Bay, SC, USA. Journal of Geophysical Research 113:C09006. Doi:10.1029/2007JC004509.

Lessa, G., 1996. Tidal dynamics and sediment transport in a shallow macrotidal estuary. In: Mixing in Estuaries and Coastal Seas, Coastal and Estuarine Studies Volume 50. Pp 338-360. American Geophysical Union.

Moskalski, S., Deschamps, A. Floc'h, F., Piete, H., Fromant, G., Verney, R., 2014. Sedimentary dynamics and geomorphological change in the Aulne estuary. Data report. Universite de Bretagne Occidentale. 170 pp.

Moskalski, S., Floc'h, F., Verney, R., Fromant, G., Le Dantec, N., Deschamps, A., 2018. Sedimentary dynamics and decadal-scale changes in the macrotidal Aulne River estuary, Brittany, France. Journal of Coastal Research. Online ahead of print February 2018. Doi: 10.2112/JCOASTRES-D-17-00126.1

Pawlowicz, R., Beardsley, B., Lentz, S., 2002. Classical tidal harmonic analysis including error estimates in MATLAB using T_TIDE. Computers & Geosciences 28, 929-937.

Pritchard, D.W., 1955. Estuarine circulation patterns. Proceedings of the American Society of Civil Engineers 81(717).

Sahin, C., Verney, R., Sheremet, A., Voulgaris, G., 2017.Acoustic backscatter by suspended cohesive sediments: Field observations, Seine Estuary, France. Continental Shelf Research 134, 39-51.

Schettini, C.A.F, Ricklefs, K., Truccolo, E.C., Golbig, V., 2006. Synoptic hydrography of a highly stratified estuary. Ocean Dynamics 56, 308-319.

Scully, M.E., Friedrichs, C.T., 2007. Sediment pumping by tidal asymmetry in a partially mixed estuary. Journal of Geophysical Research 112:C07028. Doi:10.1029/2009JC003784.

Siegle, E., Schettini, C.A.F., Klein, A.H.F., Toldo, E.E., 2009. Hydrodynamics and suspended sediment transport in the Camboriú estuary, Brazil: Pre-jetty conditions. Brazilian Journal of Oceanography 57, 123-135.

Sommerfield, C.K., Wong, K-C., 2001. Mechanisms of sediment flux and turbidity maintenance in the Delaware Estuary. Journal of Geophysical Research 116:C01005. Doi:10.1029/2010JC006462.

Tessier, C., Le Hir, P., Lurton, X., Castaing, P., 2008. Estimation de la matière en suspension à partir de l’intensité rétrodiffusée des courantomètres acoustiques à effet Doppler (ADCP). Comptes Rendus Geoscience 340, 7-67.

Thorne, P.D., Vincent, C.E., Harcastle, P.J., Rehman, S., Pearson, N., 1991. Measuring suspended sediment concentrations using acoustic backscatter devices. Marine Geology 98, 7-16.

Thorne, P.D., MacDonald, I.T., Vincent, C.E., 2014. Modelling acoustic scattering by suspended flocculating sediments. Continental Shelf Research 88, 81-91.

Thorne, P.D., Hanes, D.M., 2002. A review of acoustic measurement of small-scale sediment processes. Continental Shelf Research 22, 603-632.

Uncles, R.J., Elliott, R.C.A., Weston, S.A., 1985. Dispersion of salt and suspended sediment in a partly mixed estuary. Estuaries 8, 256-269.

Yu, Q., Wang, Y.P., Flemming, B., Gao, S., 2012. Tide-induced suspended sediment transport: Depth-averaged concentrations and residual fluxes. Continental Shelf Research 34, 53-63.

9. Figure captions

Figure 1. Map of the study area with locations of the moorings. The insets show the position of the study site within France and the Bay of Brest.

Figure 2. Relationships between the ADCP and AWAC backscatter and SSC from the YSIs, after employing the implicit iterative method. Note the saturation of the YSI values in panel 2D. There was a problem with the calibration, resulting in underprediction of the highest SSC values.

Figure 3. Relationships between SSC from the profiling YSI and SSC from the ADCP after using the implicit iterative method. Note that the calibrations were done logarithmically (in dB), whereas these plots are linear.

Figure 4. Discharge and weather data during the February deployment. A) Discharge at Châteaulin, B) Wind speed, C) Wind direction, D) Atmospheric pressure, E) Atmospheric temperature, and F) Precipitation. Weather variables are from the airport at Brest.

Figure 5. Two-day detail of water level, along-channel velocity, and SSC during the first spring tide of each deployment. A and B) Site 1 February. C and D) Site 3 February. E and F) Site 1 September. G and H) Site 3 September.

Figure 6. Dyer Flux components and related variables for Site 1 February. A) Depth-averaged velocity, B) Depth-averaged SSC, C) Dyer Fluxes F1 and F2, and Total Simple Flux, D) Dyer Fluxes F3, F4, and F5, E)

Dyer Fluxes F6 and F7, and F) Cumulative Simple Flux. Simple Flux is the product of velocity and SSC, depth-integrated and lowpass filtered. Positive flux and velocity is landward.

Figure 7. Dyer Flux components and related variables for Site 3 February. A) Depth-averaged velocity, B) Depth-averaged SSC, C) Dyer Fluxes F1 and F2, and Total Simple Flux, D) Dyer Fluxes F3, F4, and F5, E) Dyer Fluxes F6 and F7, and F) Cumulative Simple Flux. Simple Flux is the product of velocity and SSC, depth-integrated and lowpass filtered. Positive flux and velocity is landward.

Figure 8. Discharge and weather data during the September deployment. A) Discharge at Châteaulin, B) Wind speed, C) Wind direction, D) Atmospheric pressure, E) Atmospheric temperature, and F) Precipitation. Weather variables are from the airport at Brest.

Figure 9. Dyer Flux components and related variables for Site 1 September. A) Depth-averaged velocity, B) Depth-averaged SSC, C) Dyer Fluxes F1 and F2, and Total Simple Flux, D) Dyer Fluxes F3, F4, and F5, E) Dyer Fluxes F6 and F7, and F) Cumulative Simple Flux. Simple Flux is the product of velocity and SSC, depth-integrated and lowpass filtered. Positive flux and velocity is landward.

Figure 10. Dyer Flux components and related variables for Site 3 September. A) Depth-averaged velocity, B) Depth-averaged SSC, C) Dyer Fluxes F1 and F2, and Total Simple Flux, D) Dyer Fluxes F3, F4, and F5, E) Dyer Fluxes F6 and F7, and F) Cumulative Simple Flux. Simple Flux is the product of velocity and SSC, depth-integrated and lowpass filtered. Positive flux and velocity is landward.

Figure 11. Residual sediment flux components F1 through F5 as calculated by the Dyer equation and the Yu et al. (2012) model. Each datapoint is one full tidal cycle, averaged. The gray line is the one-to-one line. Symbols differentiate Sites and seasons.

Figure 12. Modeled and observed data from tidal cycle 2, Site 3 February. A) Water level; B) Depth-average velocity; C) Depth-average SSC). The results from this tidal cycle are representative of the ability of the model to replicate observed water level, velocity, and SSC.

Figure 13. The SSC gradient between Sites 1 and 3 in February.

Figure 14. Site 1 February. Comparison of depth-integrated lowpass filtered Simple Flux with total Yu Flux and three combinations of Dyer Flux components. A) regular; B) cumulative.

Figure 15. Site 3 February. Comparison of depth-integrated lowpass filtered Simple Flux with total Yu Flux and three combinations of Dyer Flux components. A) regular; B) cumulative.

Figure 16. Site 1 September. Comparison of depth-integrated lowpass filtered Simple Flux with total Yu Flux and three combinations of Dyer Flux components. A) regular; B) cumulative.

Figure 17. Site 3 September. Comparison of depth-integrated lowpass filtered Simple Flux with total Yu Flux and three combinations of Dyer Flux components. A) regular; B) cumulative.

Table 1. Sampling schedule for February and September 2013 moorings and anchor profiling.

Station	Dates	Tide (Spring/ Neap)	Activity	Instruments
1	8 Feb – 4 Mar 2013		Mooring dates	AWAC, YSI
3	11 Feb – 4 Mar 2013		Mooring dates	ADCP, YSI
1	13 Feb 2013	Spring	Profiling and samples	YSI
3	14 Feb 2013	Spring	Profiling and samples	YSI
2	25 Feb 2013	Spring	Profiling and samples	YSI
1	3 – 21 Sept 2013		Mooring dates	AWAC, YSI
3	3 – 21 Sept 2013		Mooring dates	ADCP, YSI
1	6 Sept 2013	Spring	Profiling and samples	YSI
1	9 Sept 2013	Spring	Profiling and samples	YSI
3	10 Sept 2013	Spring	Profiling and samples	YSI
1	12 Sept 2013	Neap	Profiling and samples	YSI
3	16 Sept 2013	Neap	Profiling and samples	YSI
4	18 Sept 2013	Spring	Profiling and samples	YSI
2	19 Sept 2013	Spring	Profiling and samples	YSI

Table 2. Similarity and error for relationships between SSC from the profiling YSI and SSC from the ADCP after using the implicit iterative method.

Site & season	**r^2**	**RMSE**
Site 1 February	0.148	15.01
Site 1 September	0.043	4.54
Site 3 February	0.001	178.34
Site 3 September	0.725	37.06

Table 3. Uncertainty for fluxes calculated from current profiler data.

Site and Season	Velocity accuracy	SSC error		Flux uncertainty
Site 1 February	1% of measured value	6.41 mg L^{-1}	28.1%	29.1%
Site 3 February	0.3% of measured value	73.18 mg L^{-1}	25.3%	25.6%
Site 1 September	1% of measured value	3.68 mg L^{-1}	36.2%	37.2%
Site 3 September	0.3% of measured value	23.64 mg L^{-1}	46.4%	46.7%

Table 4. The coefficients required for the expansion of Equation 16.

	$\boldsymbol{A_i/u_1^2}$	$\boldsymbol{\omega_i}$	$\boldsymbol{\gamma_i}$
E1	$-\frac{k}{u_1}\hat{u}_0+\frac{1}{2}\frac{B}{h_0}$	0	0
E2	$-\frac{k}{u_1}+2\frac{B}{h_0}\hat{u}_0-\frac{1}{2}\frac{B}{h_0}\hat{h}\cos(\varphi_{h1}-\varphi_{u1})$	ω	φ_{u1}
E3	$\frac{B}{h_0}\hat{u}_2$	ω	$\varphi_{u2}-\varphi_{u1}$
E4	$-\frac{1}{4}\frac{B}{h_0}\hat{h}$	ω	φ_{h1}
E5	$-\frac{k}{u_1}\hat{u}_2$	2ω	φ_{u2}
E6	$\frac{1}{2}\frac{B}{h_0}$	2ω	$2\varphi_{u1}$
E7	$\frac{B}{h_0}\hat{u}_2$	3ω	$\varphi_{u1}+\varphi_{u2}$
E8	$-\frac{1}{4}\frac{B}{h_0}\hat{h}$	3ω	$2\varphi_{u1}+\varphi_{h1}$

Table 5. Tidal analysis results for three sites in the Aulne.

Station	**M2 amplitude** (aM2, m)	**M2 phase** (ϕM2, deg.)	**M4 amplitude** (aM4, m)	**M4 phase** (ϕM4, deg.)	**aM4/aM2** (m)	**2ϕM2-ϕM4** (degrees)
Site 1	2.1035	139.21	0.0671	174.55	0.0319	103.87
Site 3	2.1379	116.15	0.1217	152.40	0.0569	79.9
Guily-Glaz	1.5022	150.16	0.2929	277.67	0.1950	22.65

Table 6. Wilcoxon signed rank sum test (alpha = 0.05) between Yu flux component and corresponding tidal cycle mean Dyer flux component. The null hypothesis was that there is no difference between the two flux method results. A p-value less than 0.05 means that there is a statistically significant difference between the Yu and Dyer flux results. An asterisk before the p-value indicates that the null hypothesis was rejected.

Dataset	**Flux term**	**p-value**	**z-value**	**Rank sum**	**Dataset**	**Flux term**	**p-value**	**z-value**	**Rank sum**
Site 1 Feb	F1	0.8375	-0.2051	171	Site 1 Sept	F1	0.8505	0.1884	810
Spring tides	F2	0.8375	0.2051	180	Spring tides	F2	0.3896	0.8603	851
	F3	0.7196	0.3590	183		F3	0.2160	1.2372	874
	F4	0.1998	-1.2821	150		F4	0.7123	-0.3687	775
	F5*	0.0103	2.5641	226		F5*	2.1e-9	5.9894	1164
Site 1 Feb	F1	0.8362	-0.2068	198	Site 1 Sept	F1	0.2934	-1.0506	110
Neap tide	F2	0.8005	0.2527	209	Neap tide	F2	0.1486	1.4446	149
	F3	0.8005	0.2527	209		F3	0.7928	0.2627	131
	F4	0.5657	-0.5743	190		F4	0.8955	0.1313	129
	F5	0.4763	0.7122	219		F5*	0.0488	1.9700	157
Site 3 Feb	F1	0.9705	0.0370	918	Site 3 Sept	F1	0.9173	-0.1038	736
Spring tides	F2	0.6520	-0.4509	884	Spring tides	F2	0.3502	-0.9342	688
	F3*	7.39e-11	6.5125	1356		F3*	0.0363	2.0933	864
	F4	0.1669	-1.3823	821		F4*	0.0306	-2.1625	617
	F5*	1.87e-7	5.2115	1268		F5	0.9173	-0.1038	736
Site 3 Feb	F1	0.9010	0.1244	236	Site 3 Sept	F1	0.4025	-0.8372	135
Neap tide	F2	0.9669	0.0415	234	Neap tide	F2	0.9310	0.0866	152
	F3	0.8035	-0.2489	226		F3	0.3708	0.8949	166
	F4	0.7089	-0.3733	223		F4	0.8852	0.1443	153
	F5	0.2455	-1.1614	204		F5*	0.0035	-2.9156	99

Appendix 1. Constants used during inversion of the ADCP backscatter.

Symbol	**Meaning**	**Value**
B	ADCP noise level	70 dB µPa^{-1}
SL_0	Source level emitted by current profiler	217 d dB µPa^{-1}
EC_0	Echo intensity in air (internal noise)	45 counts
Kc	Conversion coefficient	0.42 dB count^{-1}
f	Frequency of the current profiler	1200 Hz
ϑ (theta)	Beam angle	20°
φ (phi)	Beam width	3.9°
ρ_0 (rho)	Density of water	1024 kg m^{-3}
c	Speed of sound in water	Calculated from pressure, temperature, salinity
α_w (alpha)	Sound absorption by water coefficient	Calculated from pressure, temperature, salinity
ν (nu)	Kinematic viscosity of water	
ρ_s (rho)	Sediment density	2650 kg m^{-3}
c_s	Sound velocity in particles	4500 m s^{-1}
Cst	Scattering cross-section constant	-33.4212

Highlights

Moskalski et al.

1. Magnitude and direction of total residual flux change with position and discharge.
2. Eulerian flux is the main component of total flux near the mouth.
3. Tidal pumping and Stokes drift flux components gain importance landward.
4. The 6 processes in the model are insufficient to replicate residual flux in Aulne.
5. First 5 Dyer flux components were all needed to estimate total residual flux.

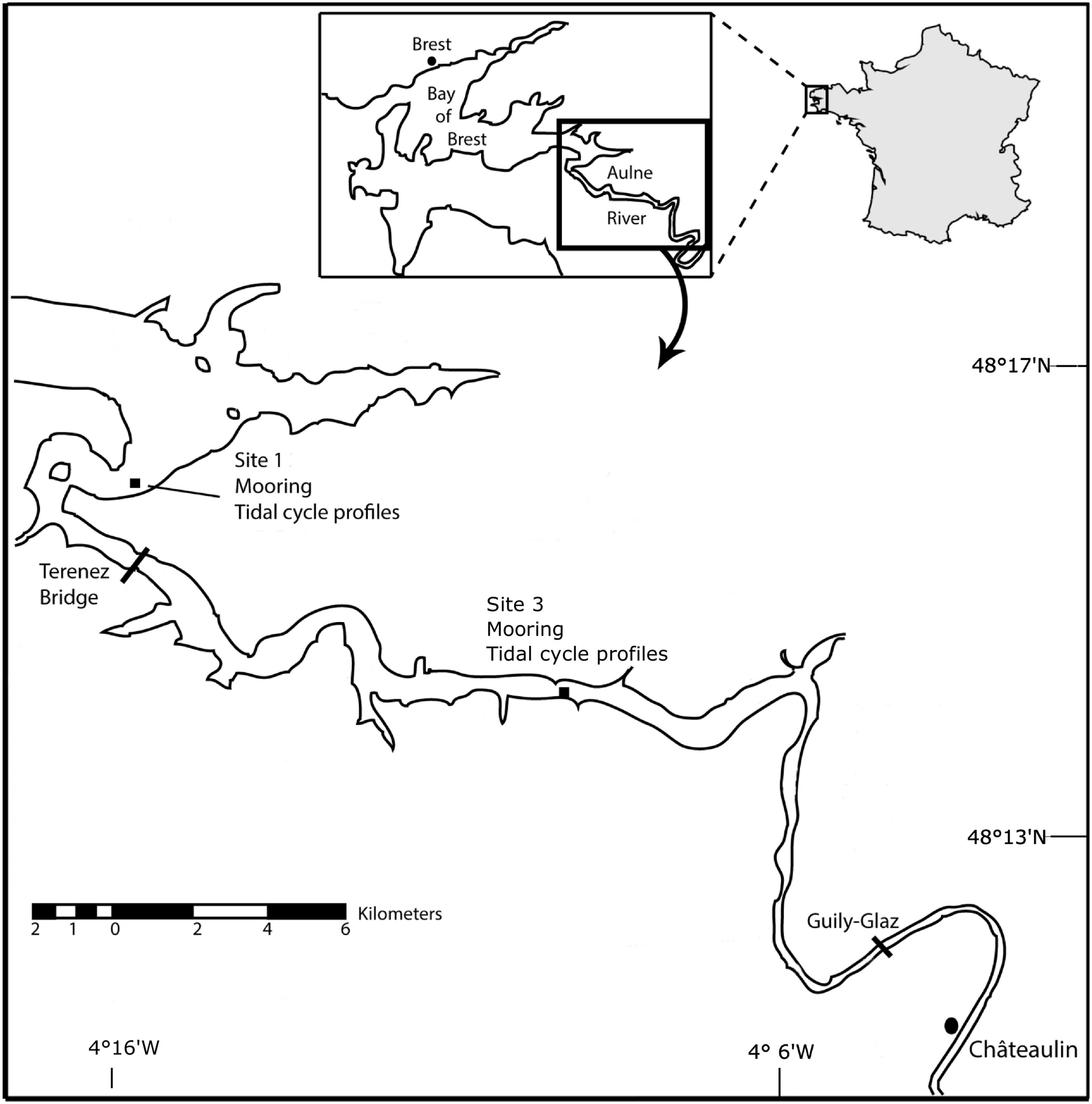
Brest
Bay
of
Brest
Aulne
River
48°17'N
Site 1
Mooring
Tidal cycle profiles
Terenez
Bridge
Site 3
Mooring
Tidal cycle profiles
48°13'N
Kilometers
2
1
0
2
4
6
Guily-Glaz
4°16'W
4° 6'W
Châteaulin

Figure 1

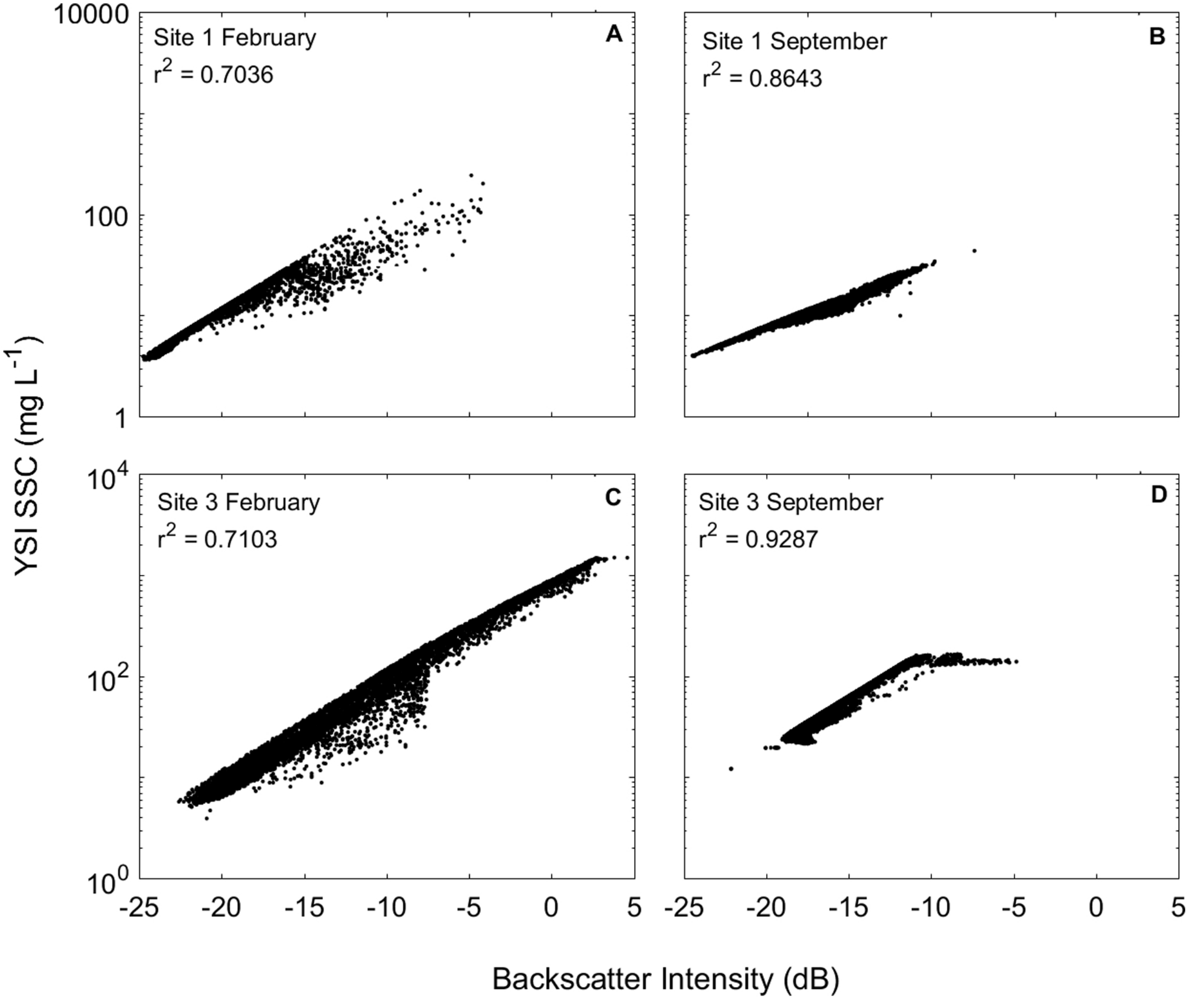
A
Site 1 February
r^2 = 0.7036
B
Site 1 September
r^2 = 0.8643
C
Site 3 February
r^2 = 0.7103
D
Site 3 September
r^2 = 0.9287
YSI SSC (mg L^{-1})
10000
100
1
10^4
10^2
10^0
-25
-20
-15
-10
-5
0
5
Backscatter Intensity (dB)

Figure 2

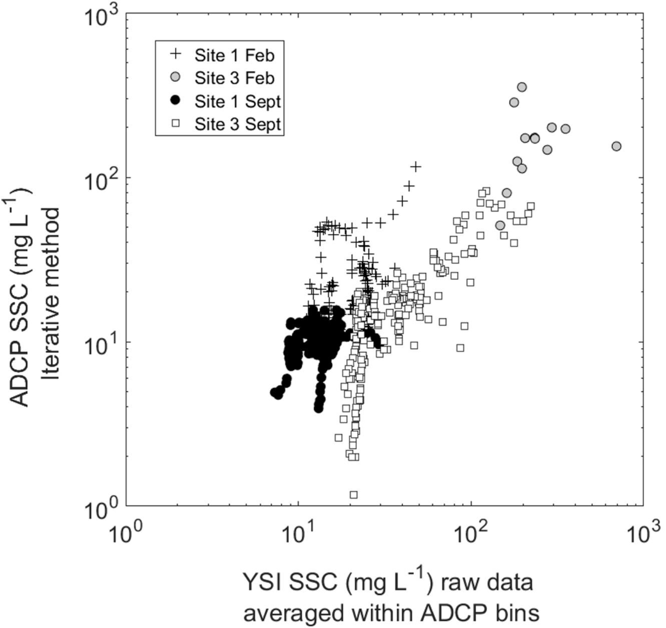
10^3
10^2
10^1
10^0
10^0
10^1
10^2
10^3
+ Site 1 Feb
● Site 3 Feb
● Site 1 Sept
□ Site 3 Sept
ADCP SSC (mg L^{-1}) Iterative method
YSI SSC (mg L^{-1}) raw data averaged within ADCP bins

Figure 3

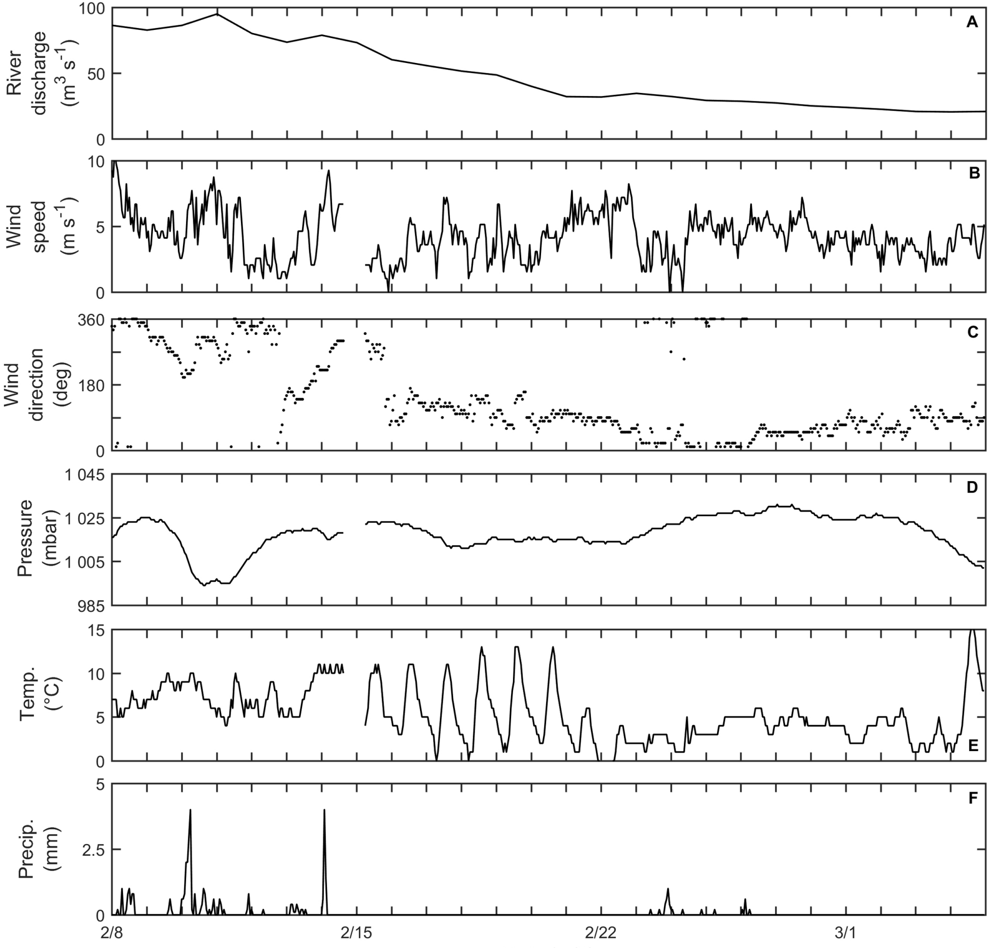

A
River discharge ($m^3 s^{-1}$)
0
50
100
B
Wind speed ($m s^{-1}$)
0
5
10
C
Wind direction (deg)
0
180
360
D
Pressure (mbar)
985
1 005
1 025
1 045
E
Temp. (°C)
0
5
10
15
F
Precip. (mm)
0
2.5
5
2/8
2/15
2/22
3/1
Date (m/d)

Figure 4

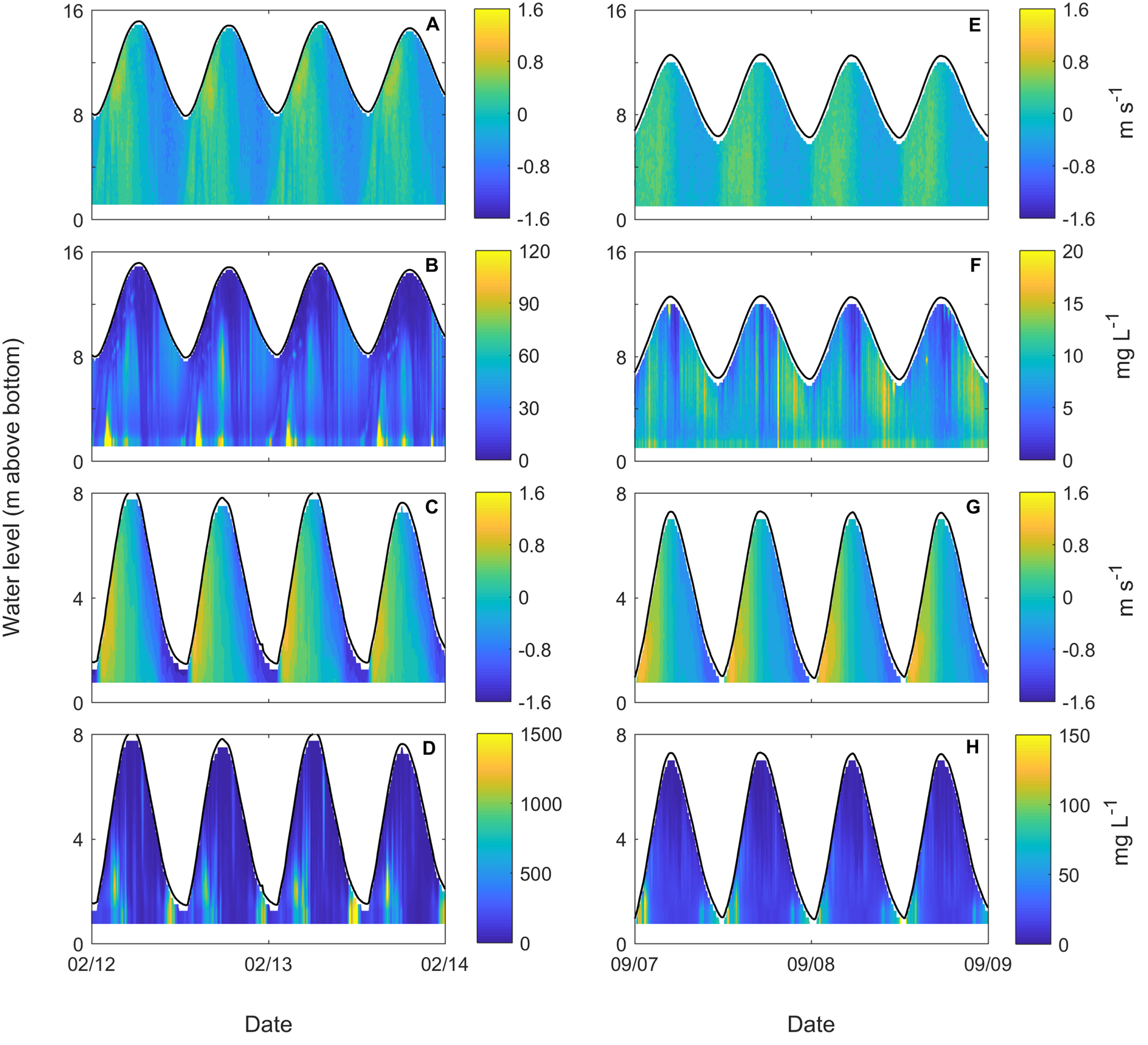
A
B
C
D
E
F
G
H
Water level (m above bottom)
16
8
0
4
1.6
0.8
0
-0.8
-1.6
120
90
60
30
1500
1000
500
20
15
10
5
150
100
50
m s-1
mg L-1
02/12
02/13
02/14
09/07
09/08
09/09
Date

Figure 5

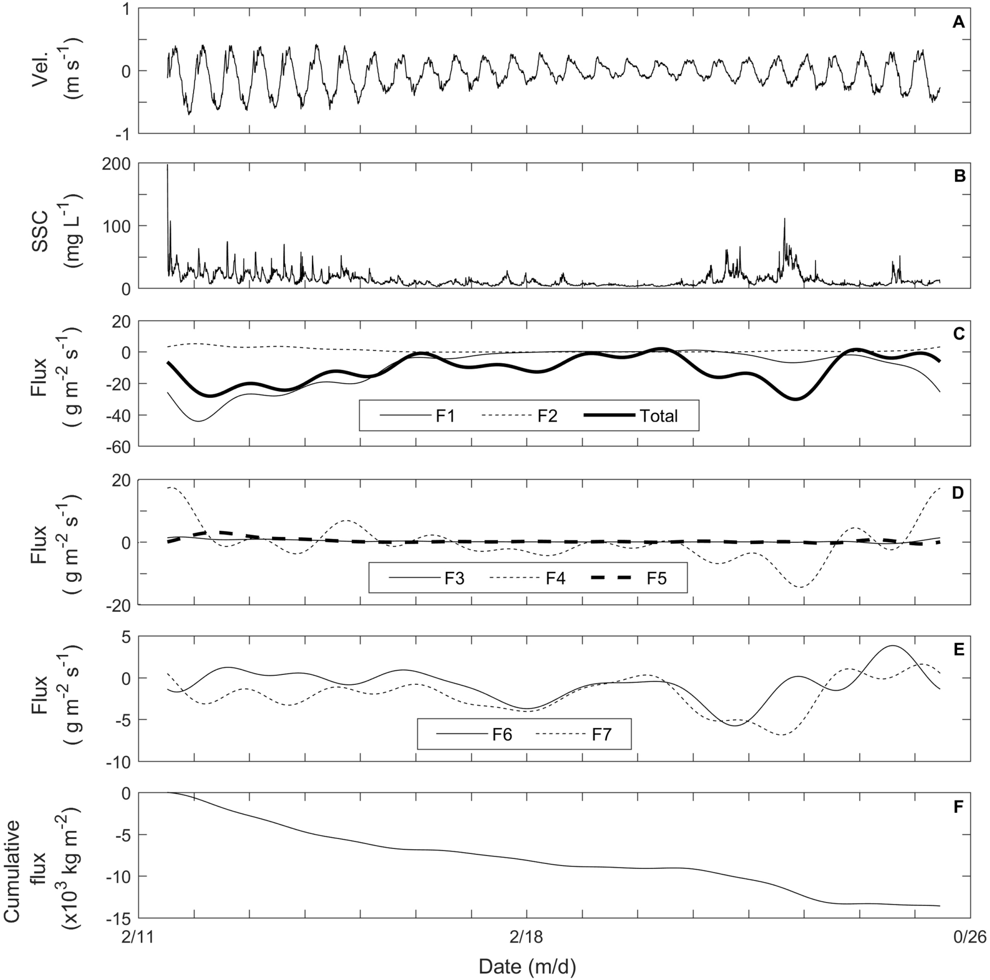

1
0
-1
Vel.
(m s-1)
A
200
100
0
SSC
(mg L-1)
B
20
0
-20
-40
-60
Flux
(g m-2 s-1)
F1
F2
Total
C
20
0
-20
Flux
(g m-2 s-1)
F3
F4
F5
D
5
0
-5
-10
Flux
(g m-2 s-1)
F6
F7
E
0
-5
-10
-15
Cumulative
flux
(x103 kg m-2)
F
2/11
2/18
0/26
Date (m/d)

Figure 6

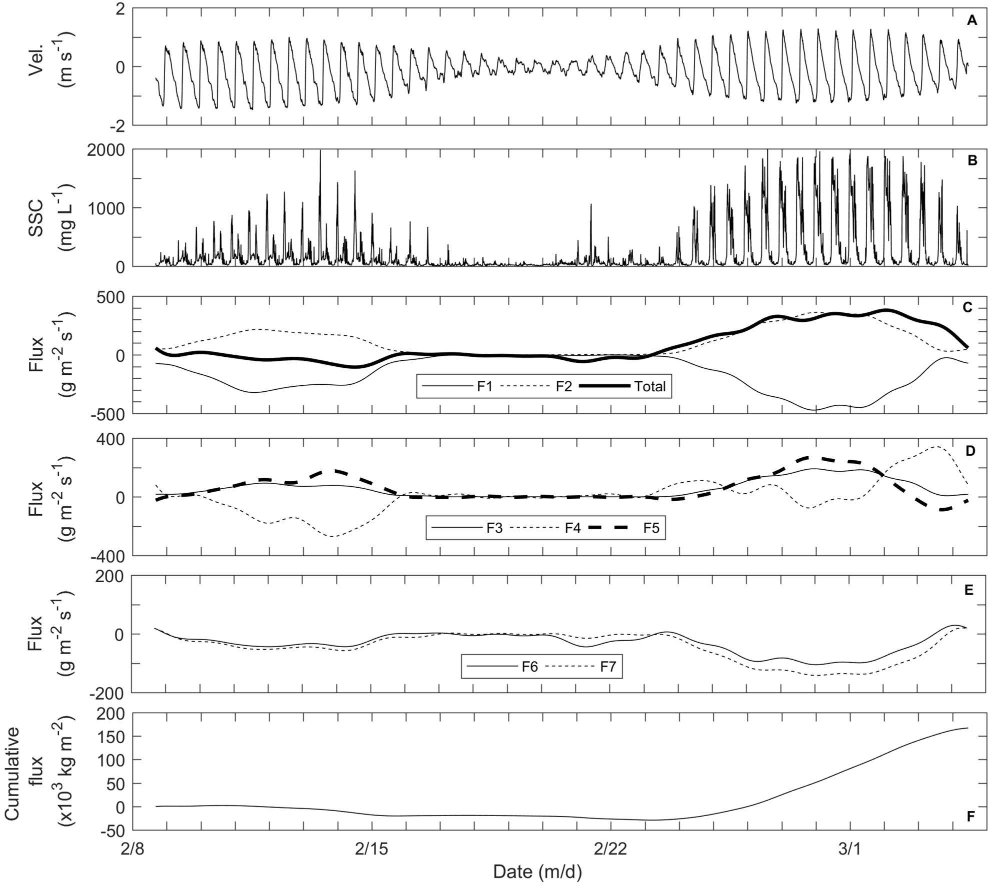
A
B
C
D
E
F
Vel. (m s^{-1})
2
0
-2
SSC (mg L^{-1})
2000
1000
0
Flux (g m^{-2} s^{-1})
500
0
-500
F1
F2
Total
Flux (g m^{-2} s^{-1})
400
0
-400
F3
F4
F5
Flux (g m^{-2} s^{-1})
200
0
-200
F6
F7
Cumulative flux (x10^3 kg m^{-2})
200
150
100
50
0
-50
2/8
2/15
2/22
3/1
Date (m/d)

Figure 7

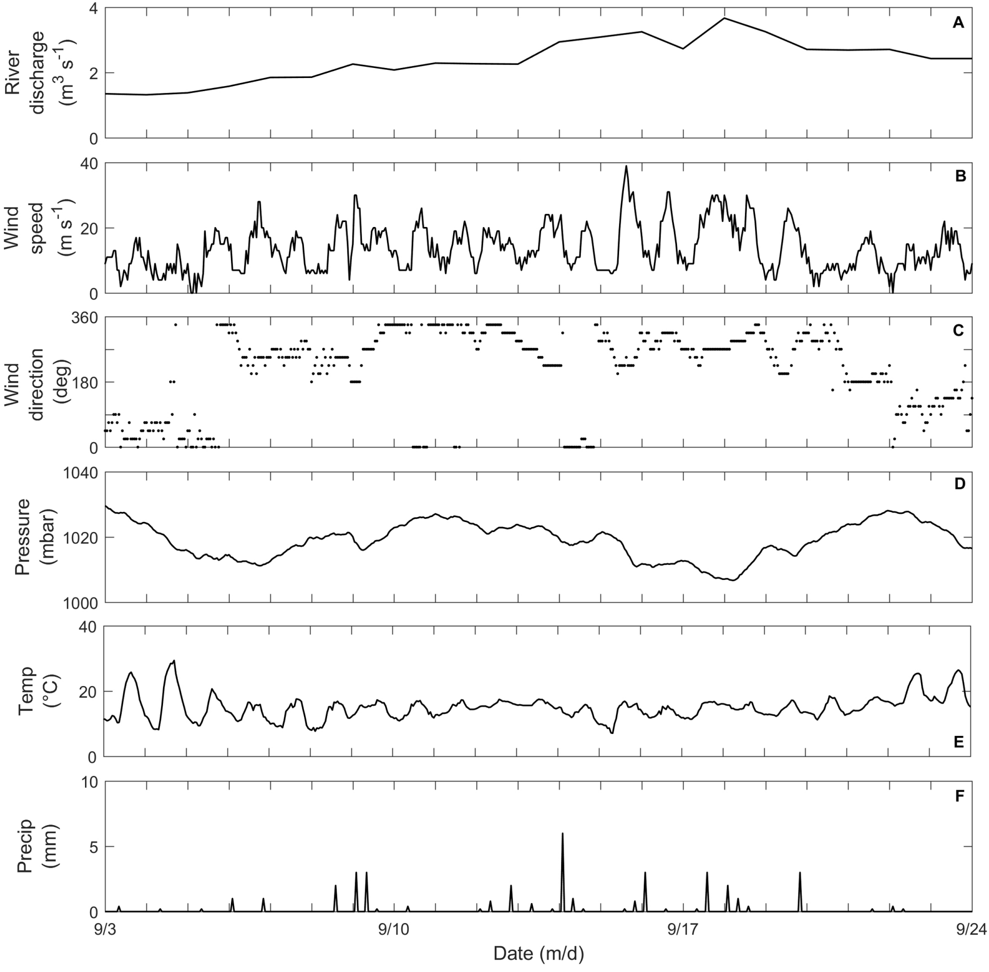
A
B
C
D
E
F
River discharge ($m^3 s^{-1}$)
Wind speed ($m s^{-1}$)
Wind direction (deg)
Pressure (mbar)
Temp (°C)
Precip (mm)
0
2
4
0
20
40
0
180
360
1000
1020
1040
0
20
40
0
5
10
9/3
9/10
9/17
9/24
Date (m/d)

Figure 8

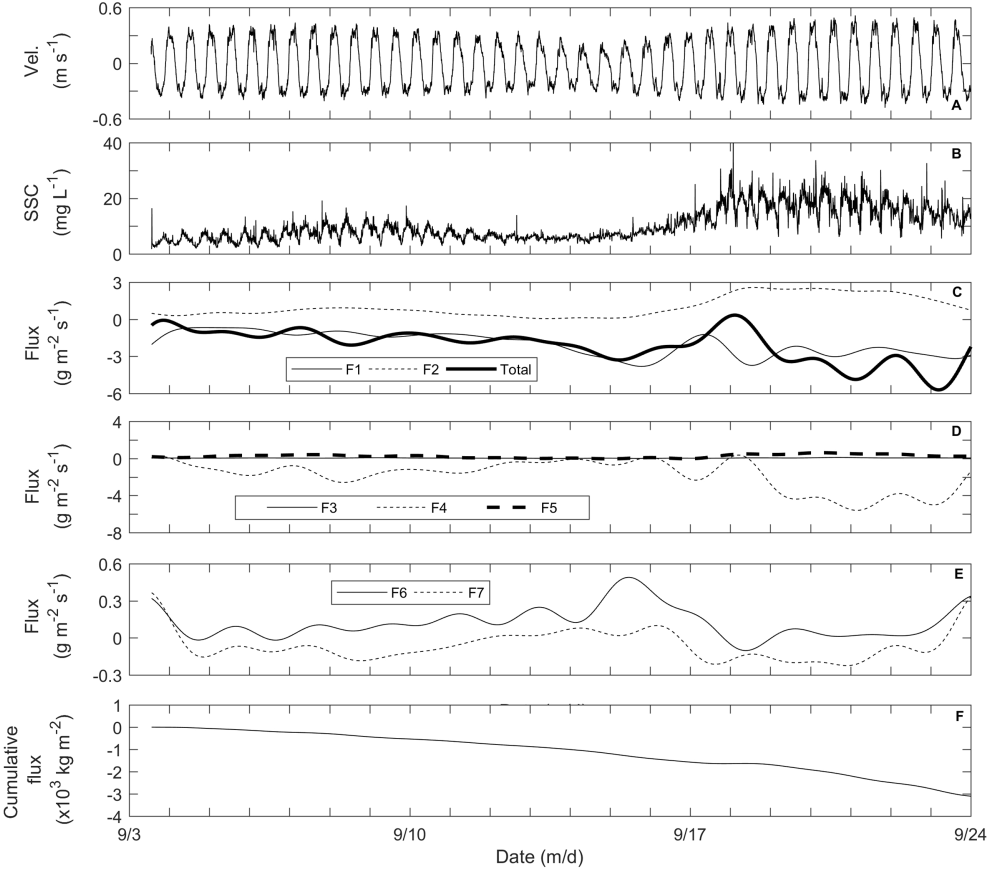

0.6
0
-0.6
Vel. (m s^{-1})
A
40
20
0
SSC (mg L^{-1})
B
3
0
-3
-6
Flux (g m^{-2} s^{-1})
F1
F2
Total
C
4
0
-4
-8
Flux (g m^{-2} s^{-1})
F3
F4
F5
D
0.6
0.3
0
-0.3
Flux (g m^{-2} s^{-1})
F6
F7
E
1
0
-1
-2
-3
-4
Cumulative flux (x10^3 kg m^{-2})
F
9/3
9/10
9/17
9/24
Date (m/d)

Figure 9

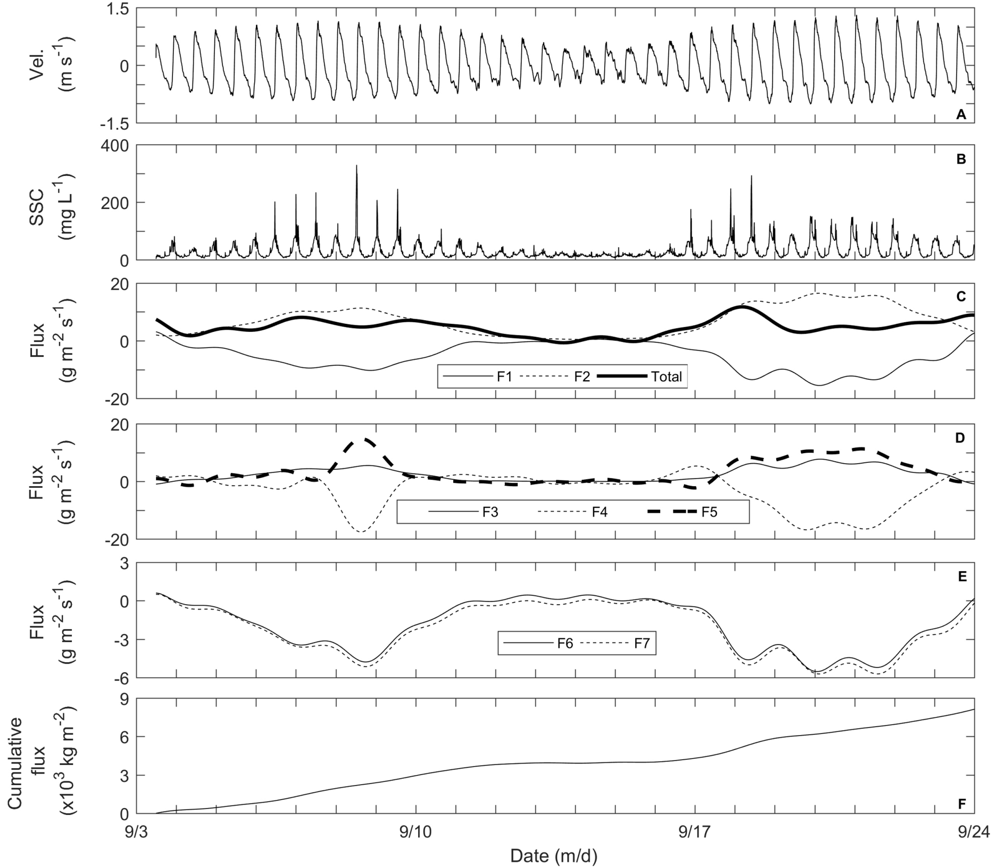

Vel. (m s^{-1})
1.5
0
-1.5
A
SSC (mg L^{-1})
400
200
0
B
Flux (g m^{-2} s^{-1})
20
0
-20
C
F1
F2
Total
Flux (g m^{-2} s^{-1})
20
0
-20
D
F3
F4
F5
Flux (g m^{-2} s^{-1})
3
0
-3
-6
E
F6
F7
Cumulative flux (x10^3 kg m^{-2})
9
6
3
0
F
9/3
9/10
9/17
9/24
Date (m/d)

Figure 10

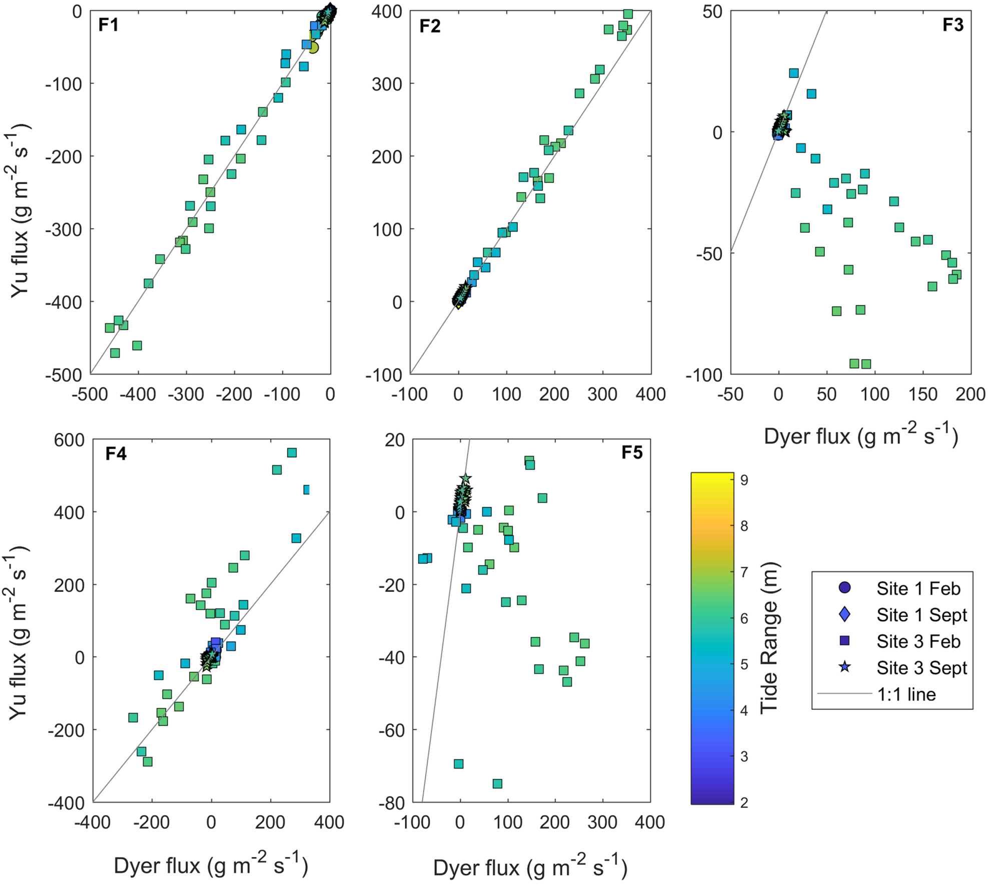
F1
F2
F3
F4
F5
Yu flux (g m^{-2} s^{-1})
Dyer flux (g m^{-2} s^{-1})
0
-100
-200
-300
-400
-500
400
300
200
100
50
-50
-100
-400
-200
0
200
400
600
20
-20
-40
-60
-80
150
Tide Range (m)
2
3
4
5
6
7
8
9
Site 1 Feb
Site 1 Sept
Site 3 Feb
Site 3 Sept
1:1 line

Figure 11

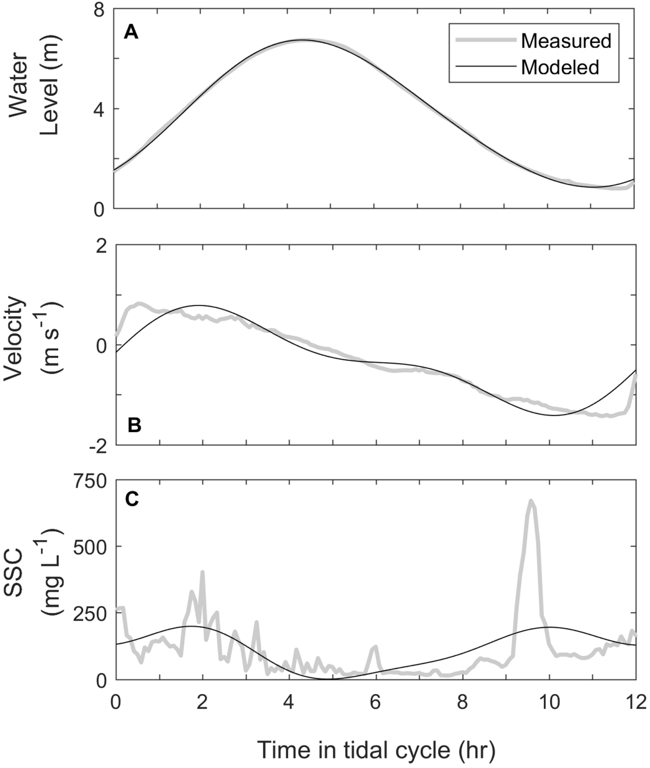
A
B
C
Measured
Modeled
Water Level (m)
Velocity (m s^{-1})
SSC (mg L^{-1})
8
4
0
2
0
-2
750
500
250
0
0
2
4
6
8
10
12
Time in tidal cycle (hr)

Figure 12

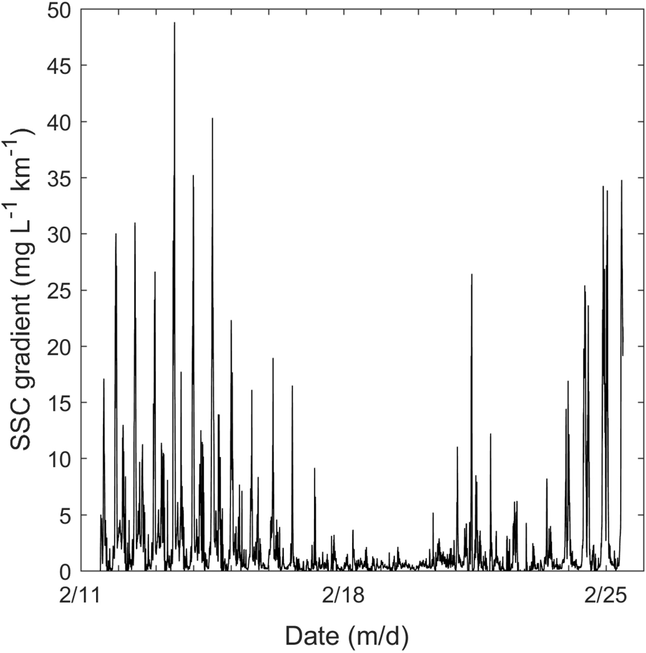

50
45
40
35
30
25
20
15
10
5
0
SSC gradient (mg L^{-1} km^{-1})
2/11
2/18
2/25
Date (m/d)

Figure 13

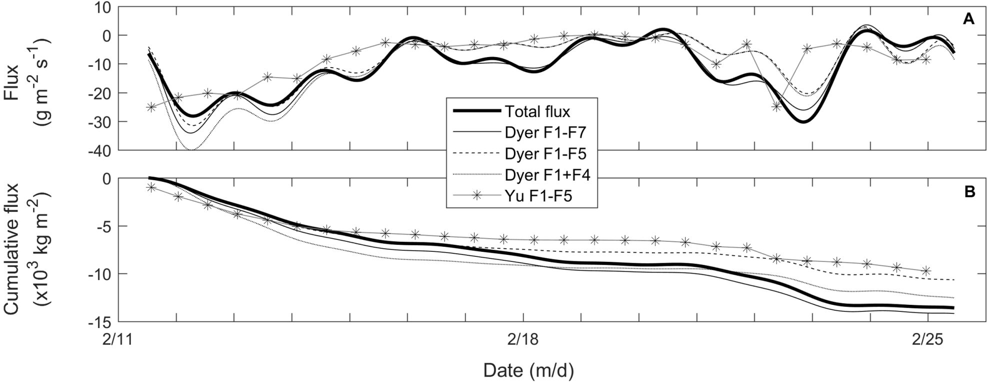
A
B
Flux
(g m^{-2} s^{-1})
10
0
-10
-20
-30
-40
Cumulative flux
(x10^3 kg m^{-2})
0
-5
-10
-15
2/11
2/18
2/25
Date (m/d)
Total flux
Dyer F1-F7
Dyer F1-F5
Dyer F1+F4
Yu F1-F5

Figure 14

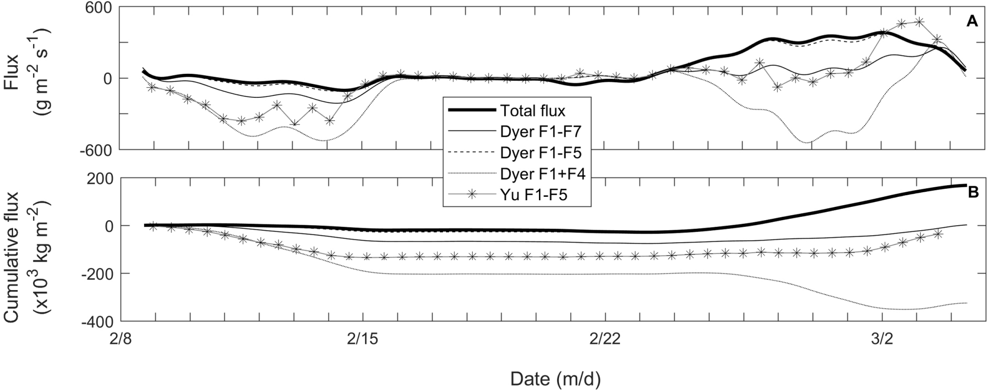
600
-600
0
Flux
(g m^{-2} s^{-1})
A
Total flux
Dyer F1-F7
Dyer F1-F5
Dyer F1+F4
Yu F1-F5
200
0
-200
-400
Cumulative flux
(x10^{3} kg m^{-2})
B
2/8
2/15
2/22
3/2
Date (m/d)

Figure 15

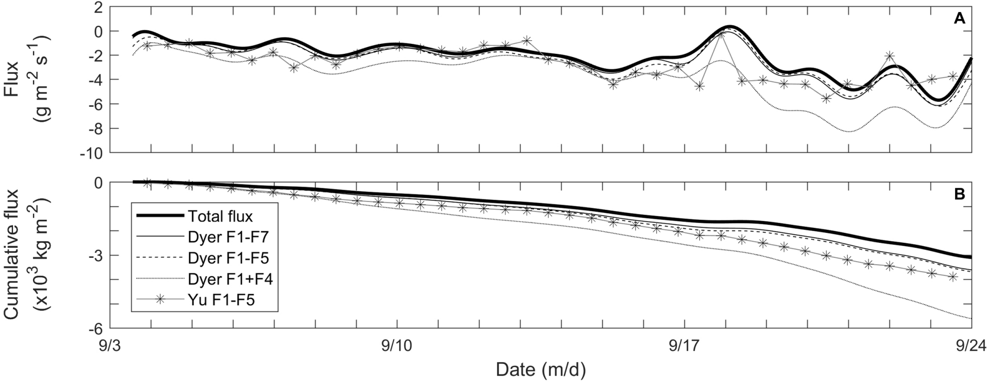
A
B
Flux (g m^{-2} s^{-1})
2
0
-2
-4
-6
-8
-10
Cumulative flux (x10^{3} kg m^{-2})
0
-3
-6
9/3
9/10
9/17
9/24
Date (m/d)
Total flux
Dyer F1-F7
Dyer F1-F5
Dyer F1+F4
Yu F1-F5

Figure 16

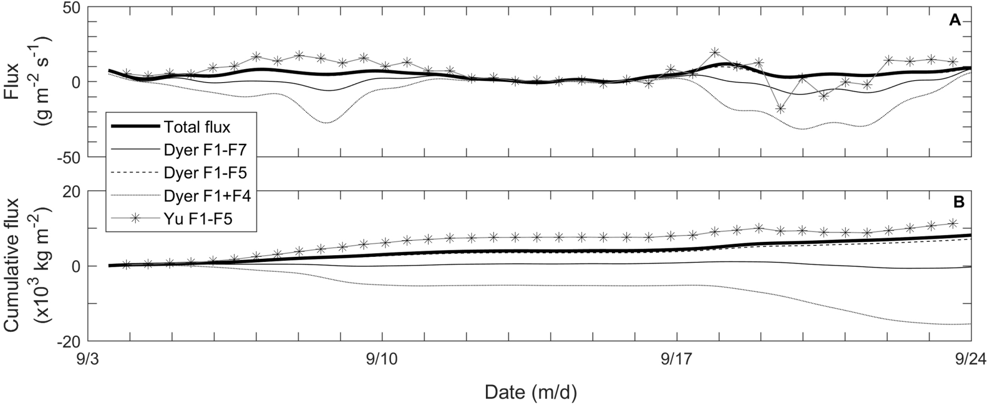
A
B
Flux
(g m^{-2} s^{-1})
50
0
-50
Cumulative flux
(x10^3 kg m^{-2})
20
0
-20
Total flux
Dyer F1-F7
Dyer F1-F5
Dyer F1+F4
Yu F1-F5
9/3
9/10
9/17
9/24
Date (m/d)

Figure 17